

PL-TR-95-2135

**REGIONAL SEISMIC EVENT
IDENTIFICATION AND IMPROVED
LOCATIONS WITH SMALL ARRAYS
AND NETWORKS**

Frank L. Vernon
J. Bernard Minster
John A. Orcutt

University of California
Scripps Institution of Oceanography
La Jolla, CA 92093-0210

20 September 1995

Final Report
7 May 1993-30 September 1995

Approved for public release; distribution unlimited



**PHILLIPS LABORATORY
Directorate of Geophysics
AIR FORCE MATERIEL COMMAND
HANSCOM AFB, MA 01731-3010**


19960322 057

SPONSORED BY
Advanced Research Projects Agency (DoD)
Nuclear Monitoring Research Office
ARPA ORDER No. A-128


MONITORED BY
Phillips Laboratory
CONTRACT No. F19628-93-K-0021

The views and conclusions contained in this document are those of the authors and should not be interpreted as representing the official policies, either express or implied, of the Air Force or the U.S. Government.

This technical report has been reviewed and is approved for publication.



JAMES F. LEWKOWICZ
Contract Manager
Earth Sciences Division



JAMES F. LEWKOWICZ
Director
Earth Sciences Division

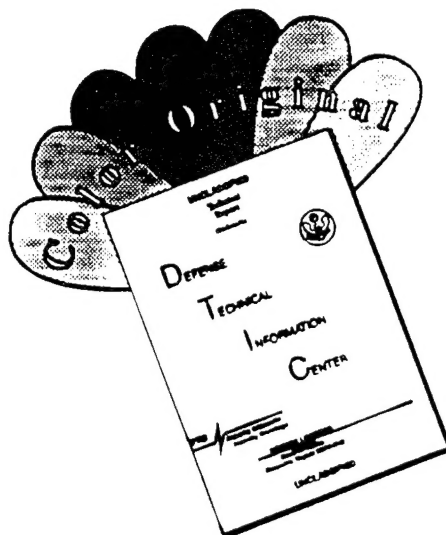
This report has been reviewed by the ESC Public Affairs Office (PA) and is releasable to the National Technical Information Service (NTIS).

Qualified requestors may obtain additional copies from the Defense Technical Information Center. All others should apply to the National Technical Information Service.

If your address has changed, or if you wish to be removed from the mailing list, or if the addressee is no longer employed by your organization, please notify PL/IM, 29 Randolph Road, Hanscom AFB, MA 01731-3010. This will assist us in maintaining a current mailing list.

Do not return copies of this report unless contractual obligations or notices on a specific document requires that it be returned.

DISCLAIMER NOTICE



THIS DOCUMENT IS BEST QUALITY AVAILABLE. THE COPY FURNISHED TO DTIC CONTAINED A SIGNIFICANT NUMBER OF COLOR PAGES WHICH DO NOT REPRODUCE LEGIBLY ON BLACK AND WHITE MICROFICHE.

REPORT DOCUMENTATION PAGE			Form Approved OMB No. 0704-0188	
Public reporting burden for this collection of information is estimated to average 1 hour per response, including the time for reviewing instructions, searching existing data sources, gathering and maintaining the data needed, and completing and reviewing the collection of information. Send comments regarding this burden estimate or any other aspect of this collection of information, including suggestions for reducing this burden, to Washington Headquarters Services, Directorate for Information Operations and Reports, 1215 Jefferson Davis Highway, Suite 1204, Arlington, VA 22202-4302, and to the Office of Management and Budget, Paperwork Reduction Project (0704-0188), Washington, DC 20503.				
1. AGENCY USE ONLY (Leave blank)		2. REPORT DATE 20 September 1995		3. REPORT TYPE AND DATES COVERED Final (7 May 1993-30 September 1995)
4. TITLE AND SUBTITLE Regional Seismic Event Identification and Improved Locations With Small Arrays and Networks			5. FUNDING NUMBERS PE 62301E PR NM93 TA GM WU AB Contract F19628-93-K-0021	
6. AUTHOR(S) Frank L. Vernon J. Bernard Minster John A. Orcutt				
7. PERFORMING ORGANIZATION NAME(S) AND ADDRESS(ES) The Regents of the University of California Scripps Institution of Oceanography IGPP 0225, 9500 Gilman Drive La Jolla, CA 92093-0225			8. PERFORMING ORGANIZATION REPORT NUMBER	
9. SPONSORING/MONITORING AGENCY NAME(S) AND ADDRESS(ES) Phillips Laboratory 29 Randolph Road Hanscom AFB, MA 01731-3010 Contract Manager: James Lewkowicz/GPE			10. SPONSORING/MONITORING AGENCY REPORT NUMBER PL-TR-95-2135	
11. SUPPLEMENTARY NOTES				
12a. DISTRIBUTION/AVAILABILITY STATEMENT Approved for public release; distribution unlimited			12b. DISTRIBUTION CODE	
13. ABSTRACT (Maximum 200 words) This final report contains a summary of our work on the use of seismic networks and arrays to improve locations and identify small seismic events. The research can be divided into three main areas. We have developed techniques to migrate 3-component array records of local, regional and teleseismic wavetrains to directly image buried two- and three-dimensional heterogeneities (e.g. layer irregularities, volumetric heterogeneities) in the vicinity of the array. The initial intent of this research effort was to identify noise sources excited by incident signals and isolate their contributions to seismic coda. This technique has been applied to small-aperture array data collected in southern California. We have developed a technique to empirically characterize local and regional seismic code by binning and stacking network recordings of dense aftershock sequences. The principle motivation for this work was to look for robust coda phases dependent on source depth. We've used these empirical results, obtained by examining ANZA network recordings of Landers and Superstition Hills aftershocks, and have developed a technique to constrain source depth. We have extended our ripple-fired event discriminant (based on the time-independence of coda produced by ripple firing) by looking for an independence of the coda from the recording direction (also indicative of ripple-firing). As part				
14. SUBJECT TERMS Small event discrimination Regional depth phases Seismic imaging			15. NUMBER OF PAGES 66	
			16. PRICE CODE	
17. SECURITY CLASSIFICATION OF REPORT Unclassified		18. SECURITY CLASSIFICATION OF THIS PAGE Unclassified		19. SECURITY CLASSIFICATION OF ABSTRACT Unclassified
				20. LIMITATION OF ABSTRACT SAR

CONT OF BLOCK 13:

of this project we have modified our sonogram code used for the expansion of time-series into time-frequency displays (used for the automatic identification of ripple-fired quarry blasts) to access data through SYBASE. The code has also been modified into the function format required by the IDC's DFX software scheme.

Contents

SITE CHARACTERIZATION WITH SMALL-APERTURE ARRAYS	1
1. INTRODUCTION	1
1.1 Deterministic Characterizations via Kirchoff Imaging	1
1.2 Locale for the Analysis	1
2. INITIAL LOOK AT DATA	1
2.1 ANZA Network and PFBA Recordings	1
3. BRIEF REVIEW OF THE IMAGING TECHNIQUE	5
4. DATA ANALYSIS	6
4.1 Imaging analysis of PFBA Data	6
5. DISCUSSION	8
6. CONCLUSIONS	9
7. ACKNOWLEDGMENTS	9
8. REFERENCES	10
EMPIRICAL CHARACTERIZATION OF REGIONAL SEISMIC CODA - CONSTRAINING DEPTH	12
1. INTRODUCTION	12
2. SYNTHETIC AND RECORDED DATA	12
2.1 Wavenumber Integration	12
2.2 ANZA Network Recordings	12
3. PRELIMINARY ANALYSIS	13
4. EVENT COLUMNS	13
5. DEPTH ESTIMATION	16
6. CONCLUSIONS	18
7. REFERENCES	20
A NEW TIME-FREQUENCY DISCRIMINANT BASED ON SIMILARITY	21
1. INTRODUCTION	21
2. DATASETS	21
2.1 A Priori Event ID	21
3. ANALYSIS OF KNET AND NRDC DATA	24
3.1 NRDC	25
3.2 KNET	26
3.3 Outliers	30
4. CONCLUSIONS AND FUTURE PLANS	30
4.1 Conclusions	30
4.2 Future Plans	30
5. REFERENCES	32
APPENDIX A. SONO	33
1. OVERVIEW	33
2. APPLICATION	33
3. REFERENCES	35
4. MISCELLANEOUS REFERENCE MANUAL PAGES	36

List of Figures

Main Body

- 1 On the left we show the PFBA (black circle) amid southern California topography and faults. The map on the lower right shows the PFBA and ANZA network stations (black triangles). The PFBA (upper right) is a 28 element 6 km aperture array which was deployed for 3 months in early 1991. Each element consists of 3 orthogonal STS-2 sensors (.0083 to 40 Hz). The Salton Trough lies to the north and east of these deployments. 2
- 2 Record section of events recorded by the vertical component of the ANZA network station PFO (located at the intersection of the crosshairs in the map). The events occurred between 0.71° and 0.78° from the station. This record section includes events at depths ranging from 0.8 to 5 km, M_l ranges from 1.9 to 3.1. Despite the similar propagation lengths these seismic records display little in common. 3
- 3 In this figure we display vertical component recordings of Landers aftershocks (above M_l 3.5) recorded by three of the ANZA network stations. The Piñon Flat station shows that an obvious phase (delayed 2 s after the onset) appears shortly before $.7^\circ$ and suggests that it disappears beyond 0.85° . The sudden appearance of this phase suggests that it is a bounce from the Moho that reaches the critical angle by 0.7° . The other two stations suggest that the energy is not due to a simple bounce since there is little evidence of a late phase at these locations. 4
- 4 Vertical component triggered-mode recordings of an event (91057061428.22) that occurred roughly 85 m to the northeast of the array. Note the phase arriving 2.25 s after the onset energy. The recordings have been band-passed between 4 and 6 Hz. 6
- 5 3-component image calculated using event 91057061428.22 on the vertical trending 14° East of North. Energy is concentrated at a depth of 30 km roughly 20 to 30 km to the north of the PFBA. 7
- 6 Three dimensional image calculated using event 91057061428.22. Note the distribution of energy in space along the 2.25 s isotime curve. The beaded nature of the energy distribution is an artifact of the gridding end with and is not due to sidelobes in the Impulse Response. 8
- 7 Landers and Superstition Hills aftershocks are shown on the left (with ANZA network stations represented by the triangles). On the right are the two aftershock sequences in range and depth. 13
- 8 On the upper left we show a vertical suite of WI earthquake synthetics. Superimposed on the synthetics are travel time curves for pP, sP, pPmP and sPmP. On the upper right we show the same traces after conversion to envelopes. On the bottom we show the travel time curves resulting from binning sources in range from 0.8 to 0.9° . The binning has the most significant affect on the PmP phases. 14
- 9 An event column based on Landers aftershocks occurring 0.9 to 1.1° from the station. Superimposed on this figure are travel time curves for pP, sP, pPmP and sPmP. To the right is a histogram indicating the number of recordings in each bin. 15
- 10 This figure is the same as Figure 9 except it uses Landers aftershocks located 0.8 to 0.9° from the station. 16
- 11 This figure is the same as Figure 9 except it uses Superstition Hills aftershocks located 0.8 to 0.9° from the station. 17

- 12 All single- to master-trace cross correlations are shown here (for the event 18
columns shown in Figures 9 and 10) and are represented by the triangles. The
squares represent the best single-station cross-correlations (i.e. the single-station
depth solutions). These solutions cluster around a zero residual.
- 13 ANZA network depth residuals obtained using the event columns displayed in 19
Figures 9 and 10.
- 14 The NRDC and KNET deployments. The NRDC figure shows event locations. 22
The highlighted events include CH1 and CH2 (the calibration explosions) and
EVC (a quarry blast).
- 15 Two sonograms (with time-series) calculated using NRDC recordings. On the 23
top is the sonogram of CH2 recorded at Bayanaul. On the bottom is the
sonogram of EVC also recorded at Bayanaul.
- 16 Four binary sonograms calculated using NRDC recordings. On the top row are 24
binary sonograms calculated using the recordings displayed in Figure 15. CH2 is
on the left, EVC is on the right. On the bottom row are binary sonograms of EVC
calculated using the N-S and E-W Bayanaul recordings.
- 17 The results of applying the similarity discriminant to the NRDC dataset. In this 25
figure events 1 to 15 are believed to be quarry blasts, 16 to 18 are the calibration
explosions. On the left we show single station solutions, the full network
solutions (using the borehole high-gain channel) are shown on the upper right
(with the number of stations displayed below).
- 18 The KNET and the events used in Figures 19 to 21. The three circles represent 26
the three event populations. The upper right circle encloses the limestone quarry
location that gave rise to the 50 quarry blasts used in the calibration and testing of
the similarity discriminant. In the circle on the lower left are the earthquakes
(aftershocks to the Mw 7.4 Suusamyrt thrust earthquake) used in calibrating the
discriminant in this area. The middle circle encloses the earthquakes that were
used to test the discriminant.
- 19 Single station solutions and ranges. Events 1 to 25 are believed to be quarry 27
blasts. The remaining events are aftershocks to the Suusamyrt thrust event.
- 20 Network solutions using the same (calibration) events considered in the preceding 28
figure. On the bottom we display the number of stations used in each solution.
The earthquake solutions follow a normal distribution. The horizontal lines
represent the mean and $\pm 1, 2$ and 3 standard deviations.
- 21 Network solutions using the test events (see Figure 18). The horizontal lines in 29
the top figure are reproduced from Figure 20 (the calibration events).

Appendix

- A1 Geographic locations of receivers and events in the 1989 NRDC dataset. 49
- A2 Seismogram resulting from the single-chemical explosion Chemex 2 recorded at a 50
range of 157 km by the vertical component surface seismometer at Bayanaul and
corresponding sonogram.
- A3 Seismogram resulting from event c recorded at a range of 264 km by the vertical 51
component surface seismometer at Bayanaul and corresponding sonogram. This
event is believed to be ripple fired. The sonogram matrix contains a clear time-
independent spectral signature.

- A4 Original spectral estimate (solid) and two filtered versions, one relatively 52
unsmoothed (fine dash) and the other heavily smoothed (coarse dash). This
figure is intended to illustrate the means by which we reduce each spectral
estimate to a binary spectral estimate. In the following figures regions of locally
high power are represented by a +1 (white). Regions deficient in power are
represented by a -1 (black).
- A5 Vertical component binary sonogram matrix corresponding to Chemex 2 recorded 53
at Bayanaul (see Figure A2). The first 35 seconds of coda after the compressional
onset are represented in this and the next binary sonogram.
- A6 Vertical component binary sonogram matrix corresponding to event c recorded at 54
Bayanaul (see Figure A3). Note the clear time-independent pattern.

Site Characterization with Small-Aperture Arrays

1. INTRODUCTION

An important aspect of nuclear monitoring is to understand the generation of seismic coda, particularly the near-station mechanisms. In some instances, secondary arrivals, due to near station processes (incl. scattering from two- or three-dimensional heterogeneities), may be incorrectly interpreted as direct arrivals, including so-called "depth phases", particularly when they are detected by single stations. Studies quantifying the effects of scattering have mostly been statistical and have dealt with the influence of small-scale random scatterers (e.g. Aki, 1969, Aki & Chouet, 1975). Some deterministic studies (Key, 1967; Key, 1968; Gupta et al., 1990; Gupta, Lynnes & Wagner, 1990; Bannister, Husebye & Ruud, 1990; Lay, 1987; Lynnes & Lay, 1989; Hedlin et al, 1994 Revenaugh, 1995) have produced compelling evidence that large crustal inhomogeneities or topographic features are capable of producing significant amounts of scattered energy, often in the form of large, identifiable seismic phases.

1.1 Deterministic Characterizations via Kirchoff Imaging

Assuming that the velocity structure of the Earth volume of interest is reasonably well constrained and that the seismic signals scattered from prominent heterogeneities are recorded by a spatial deployment of seismometers it should be possible to "reverse" the propagation and *image* the points at which the energy was scattered and re-directed toward the recording station(s). There are a number of *classic* imaging techniques available to "de propagate" scattered energy. Surface integration or Kirchoff techniques are widely used by Oil Exploration firms to process seismic reflection data and probe the sub-surface for hydrocarbon bearing structures or strata. In essence the velocity model is used to predict when, at a given station, a scattered arrival should be expected from a particular location in the Earth. By predicting arrival times at all recording stations and integrating the appropriate portions of the records, any phases arriving from a particular location in the Earth can be constructively interfered and enhanced. By systematically repeating this time-shifting and integration process for small sub-volumes within a volume of interest prominent scatterers, or heterogeneities, can be imaged.

1.2 Locale for the analysis

For this work we have chosen seismic recordings made in a structurally complex area - southern California. Although most previous deterministic analyses have focused on scattering at the free-surface, in this work we scan the entire crustal volume near the receiving station in search of prominent scatterers. Although multiple scattering and the chance coincidence of energy from small scale scatterers can give rise to prominent coda phases, this study that we will be describing specifically seeks the product of single-discrete scattering interactions at intermediate (1 to 10 Hz) frequencies.

2 INITIAL LOOK AT DATA

2.1 ANZA network and PFBA recordings

Before discussing our attempts to deterministically associate specific coda phases with specific locations in the Earth we'll conduct a brief review of time series recorded in the area of current interest. In this paper we are looking at local recordings of seismic events in southern California made by two deployments. The ANZA broadband network is a 10 station 3-component network that utilizes STS-2 broadband sensors and 24-bit dataloggers generating triggered (250 sps) and continuous (20 sps) data

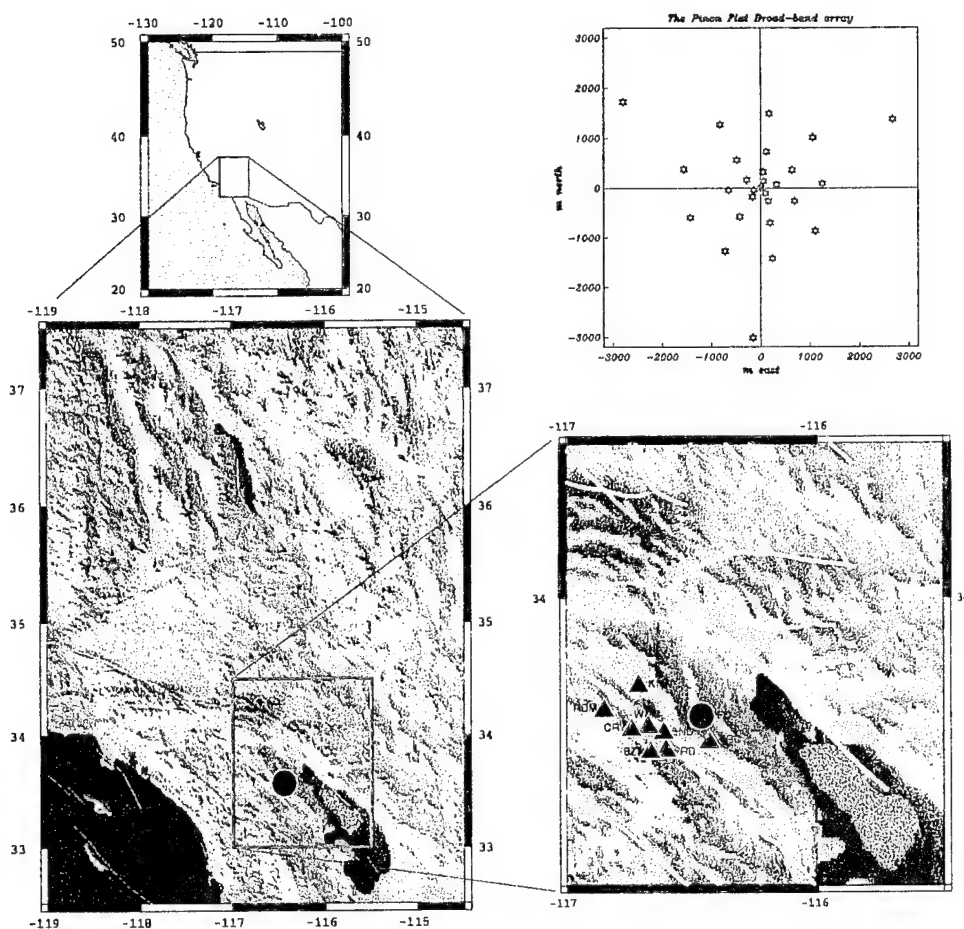


Figure 1: On the left we show the PFBA (black circle) amid southern California topography and faults. The map on the lower right shows the PFBA and ANZA network stations (black triangles). The PFBA (upper right) is a 28 element 6 km aperture array which was deployed for 3 months in early 1991. Each element consists of 3 orthogonal STS-2 sensors (.0083 to 40 Hz). The Salton Trough lies to the north and east of these deployments.

streams. The network is located in the Peninsular Ranges batholith in southern California and was emplaced to monitor local and regional seismicity in southern California (Figure 1). This location has proven to be particularly useful since the batholith provides exceptionally low-loss and homogeneous transmission paths (by California standards). The network station at the Piñon Flat Observatory (PFO) is particularly useful since it is deployed at the site that was used for a temporary array, the Piñon Flat Broadband Array (PFBA). The PFBA was deployed during the winter months of 1991 and consisted of 28 stations located in concentric rings with a maximum aperture of 6 km (Figure 1). Each station in the array was comprised of 3 orthogonal broadband (0.0083 to 40 Hz) sensors. During its short life the array made triggered (100 sa/s) recordings of 130 local and 140 regional and teleseismic events as well as continuous (20 sa/s) recordings of these, and other smaller, events.

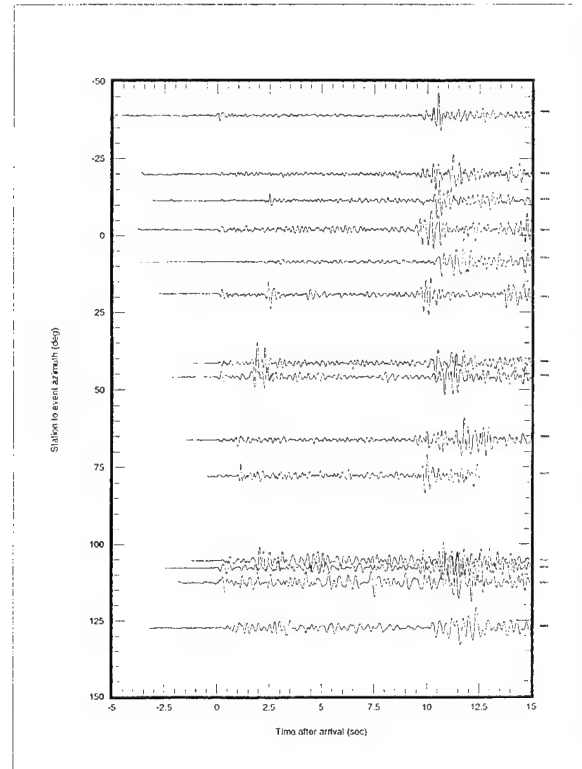
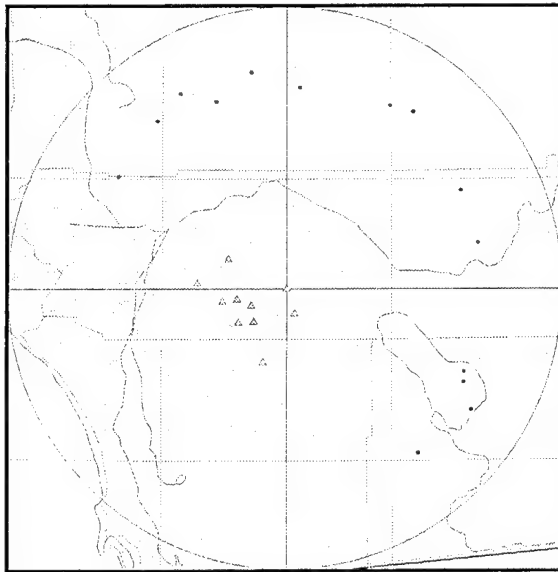
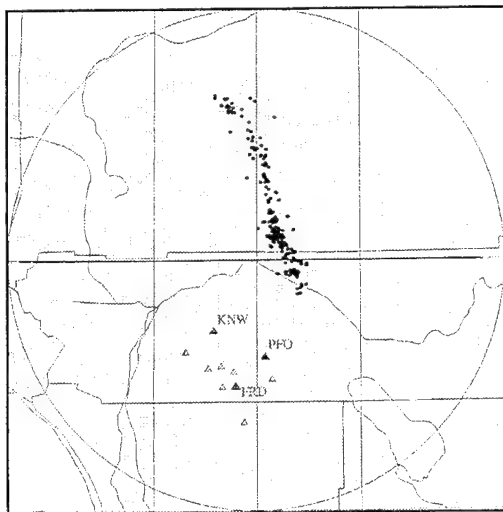


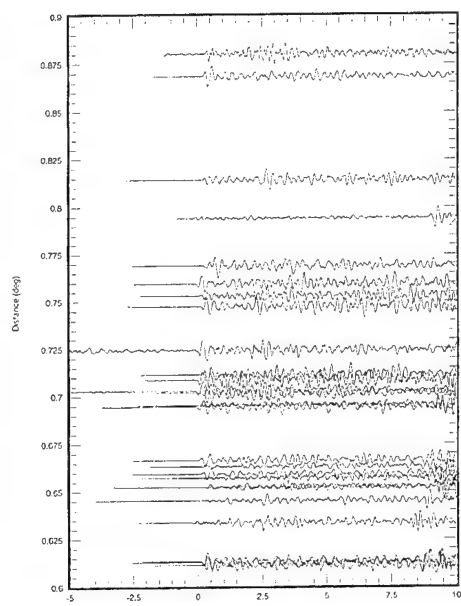
Figure 2: Record section of events recorded by the vertical component of the ANZA network station PFO (located at the intersection of the crosshairs in the map). The events occurred between 0.71 and 0.78° from the station. This record section includes events at depths ranging from 0.8 to 5 km, M_L ranges from 1.9 to 3.1 . Despite the similar propagation lengths these seismic records display little in common.

For an initial look at waveforms we display (in Figure 2) vertical component recordings of local events made by the network station at PFO. This figure contains events that occurred between 0.71 and 0.78° from PFO at depths ranging from $.8$ to 5 km and had local magnitudes of 1.9 to 3.1 . The time series, which are aligned on the first arrivals, are remarkably dissimilar. Some records (for example those at a back azimuth from PFO of 35°) contain a discrete high-amplitude arrival roughly 2 s after onset. Other events contain a similar arrival elsewhere in the P wave coda (*e.g.* earlier at a back azimuth of 75°). Some events contain no distinct coda phases. Some differences could be due to variations in the Moho depth, differences in event range from PFO, depth or focal mechanism. Examination of this figure alone might lead one to conclude that the high amplitude coda phases are simply near-critical Moho reflections; however, a closer look at the data suggests otherwise.

The ANZA network made triggered and continuous mode recordings of the Landers event and 158 aftershocks above $M 4.0$ (Figure 3). This linear aftershock trend gives us an opportunity to view the behavior of coda phases with range since the ANZA network stations recorded the events at ranges from 0.2 to 1.2° . It is likely that the aftershocks have similar focal mechanisms. In Figure 3 we show record sections of aftershocks ranging from 0.6 to 0.9° from three stations in the network (KNW, FRD and PFO). Although there is some indication of a late phase in the KNW and FRD record sections only the PFO records consistently contain a bright coda phase. This phase appears to “turn on” at roughly

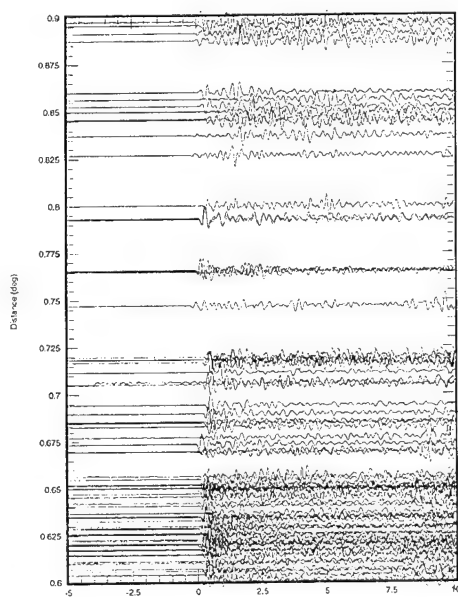


KNW EHZ



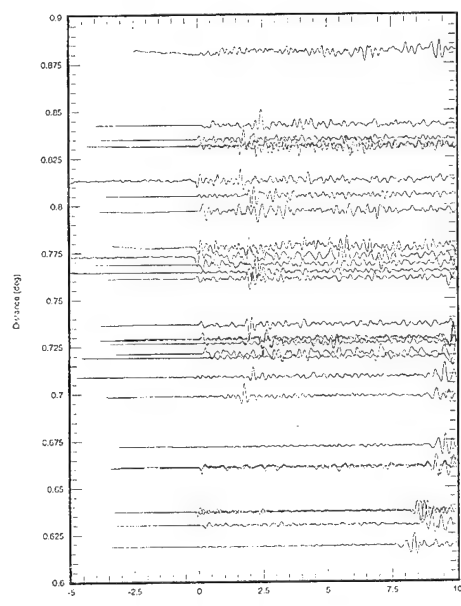
Filter: BW 0.05 4
JSPC dbrsec:mike_landers_anza dbrsec:mike_landers_anza.1.pe vernon Wed Nov 30 08:43:24 1994

FRD EHZ



Filter: BW 0.05 4
JSPC dbrsec:mike_landers_anza dbrsec:mike_landers_anza.1.pe vernon Wed Nov 30 08:53:55 1994

PFO HHZ



Filter: BW 0.05 4
JSPC dbrsec:mike_landers_anza dbrsec:mike_landers_anza.1.pe vernon Wed Nov 30 08:35:48 1994

Figure 3 In this figure we display vertical component recordings of Lander aftershocks (above M_L 3.5) recorded by three of the ANZA network stations. The Piñon Flat station shows that an obvious phase (delayed 2 s after the onset) appears shortly before 0.7° and suggests that it disappears beyond 0.85° . The sudden appearance of this phase suggests that it is a bounce from the Moho that reaches the critical angle by 0.7° . The other two stations suggest that the energy is not due to a simple bounce since there is little evidence of a late phase at these locations.

0.7° and might not be present beyond 0.85°. Not only is this phase capricious among events distributed azimuthally but also among events distributed in range. Furthermore, depending on where an event is recorded the phase might, or might not, be present.

Although the PFBA was deployed after the Landers aftershock sequence this array recorded some of the events considered in Figure 2, including the two mentioned above located at a back azimuth of 35°. An f - k analysis of PFBA recordings of events located to the northeast of the array/network (summarized in *Hedlin & Vernon, 1995*) show that the onset phase crosses the array from the azimuth of the source at a phase velocity of 6 to 7 km/s while the later phase crosses with an approach angle biased to the north at a phase velocity of 10 to 11 km/s.

This preliminary look at data has given us some idea of the extreme complexity of local coda recorded in southern California and has led to several questions: 1) Why do some local coda contain bright phases while others, from nearby events, do not? 2) Why do certain stations seem to receive bright coda phases while others, nearby, do not? 3) Why do these late phases sometimes arrived from biased directions? To further our understanding of these coda phases we will use the 3-component PFBA to scan the crust and upper mantle and image the point(s) at which they are redirected toward the receiver.

3. BRIEF REVIEW OF THE IMAGING TECHNIQUE

In calculating images of crustal scatterers we follow a simple hypothesis. We invoke the first Born approximation and thus assume that coda energy is solely due to single scattering at locations within the Earth or at the surface. By following this assumption in our processing we suppress contributions made to coda by higher order scattering. We are deliberately attempting to deterministically characterize single scattering at the more prominent crustal scatterers or interfaces. Initial versions of this technique have been described in earlier papers (*Hedlin, 1991; Hedlin et al. 1991, 1994*) and so only a brief review and a summary of the improvements will be given here. In our analysis of free-surface scatterers in southern Norway we used single (vertical) component station recordings of teleseisms made by the small-aperture NORESS array. Imaging the region surrounding the array was accomplished simply by conducting a systematic (grid) search for scatterers. At each point we would beamform for scattered waves coming from the candidate scatterer and use simple travel time calculations to predict where in the array records any scattered waves should appear. In essence we assume that a scatterer exists at a location in a grid and then we stack the records to constructively interfere single-scattered signals. This approach is a time-surface integration, or Kirchoff migration, technique (*Yilmaz, 1987*). *Hedlin et al. (1991; 1994)* used a similar approach to image P to R_g scatterers in Norway and found evidence that energy was being scattered at sharp topographic relief.

In this paper we extend our earlier work in several ways. Instead of restricting our analysis to surface scatterers excited by teleseismic wavetrains we have adapted the technique to accommodate scatterers located anywhere in a layered earth excited by local, regional or teleseismic events. We have introduced a polarization analysis into the technique that takes advantage of 3-C array data. To backproject the energy into a volume of the crust we look at individual sub-volumes in sequence. Raytracing through an assumed Earth model associates each sub-volume with a propagation vector and with the appropriate time delay that should exist between the parent and a single-scattered phase. The 3-component array data are then tuned to this vector by steering each 3-component station for the direction of particle motion of interest (*e.g.* longitudinal, transverse) and then through beamforming these steered channels are summed together to yield a single trace dedicated to energy propagating from the subvolume.

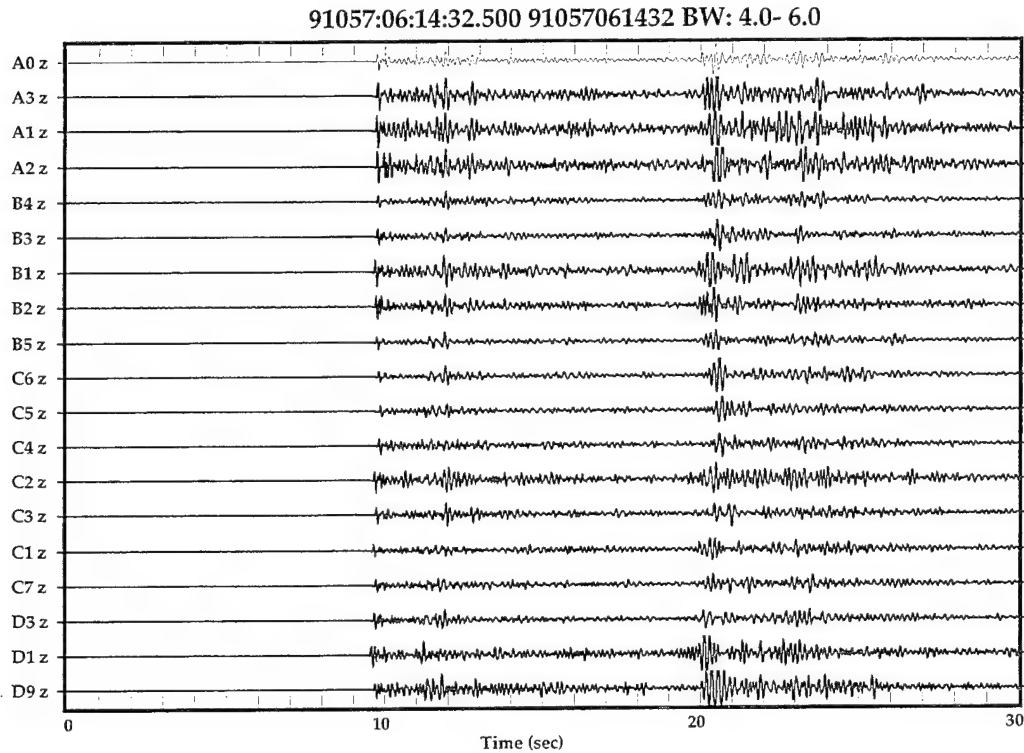


Figure 4: Vertical component triggered-mode recordings of an event (91057061428.22) that occurred roughly 85 m to the northeast of the array. Note the phase arriving 2.25 s after the onset energy. The recordings have been band-passed between 4 and 6 Hz.

The time-delay calculated for the sub-volume determines the portion of the tuned time-series that is attributed to it. This process, which is akin to Kirchhoff migration, yields an image of coherent, first-order scatterers that exist within the Earth or at the free surface. Having 3-component data obviates the need for an obliquity factor that is used when Kirchhoff migration is applied to vertical component reflection data (Yilmaz, 1987). To date we have restricted the analysis to 1-Dimensional Earth models and apply the appropriate geometrical spreading factor.

4. DATA ANALYSIS

4.1 Imaging analysis of PFBA data

To demonstrate this technique we'll consider the bright coda phase discussed in section 2. We have analyzed triggered and continuous mode recordings of local and regional events that occurred to the northeast of the array. One event (which occurred on day 057) occurred 85 km from the array at a back-azimuth of 35° . The *P* and *S* onsets occur at roughly 10 and 20 s respectively. The coda contains a significant phase delayed 2.25 s after the *P* wave onset (Figure 4). As discussed in section 2 f-k analysis indicates that the onset phase arrives from the azimuth of the event, at a phase velocity of 6.2 km/s while the later phase arrives from a back azimuth of 14° at 12 km/s. In Figure 5 we show a profile through the crust that passes through the array and bears 14° East of North. In the upper figure we display the time delays we predict should exist between the arrivals of the energy directly from the event and via single P-P scattering interactions that occur in this vertical plane. Given that our assumptions (regarding the velocity model and the scattering) are reasonable the source of the late energy should lie somewhere on the 2.25 s curve (dashed). The middle third of Figure 5 shows the slowness

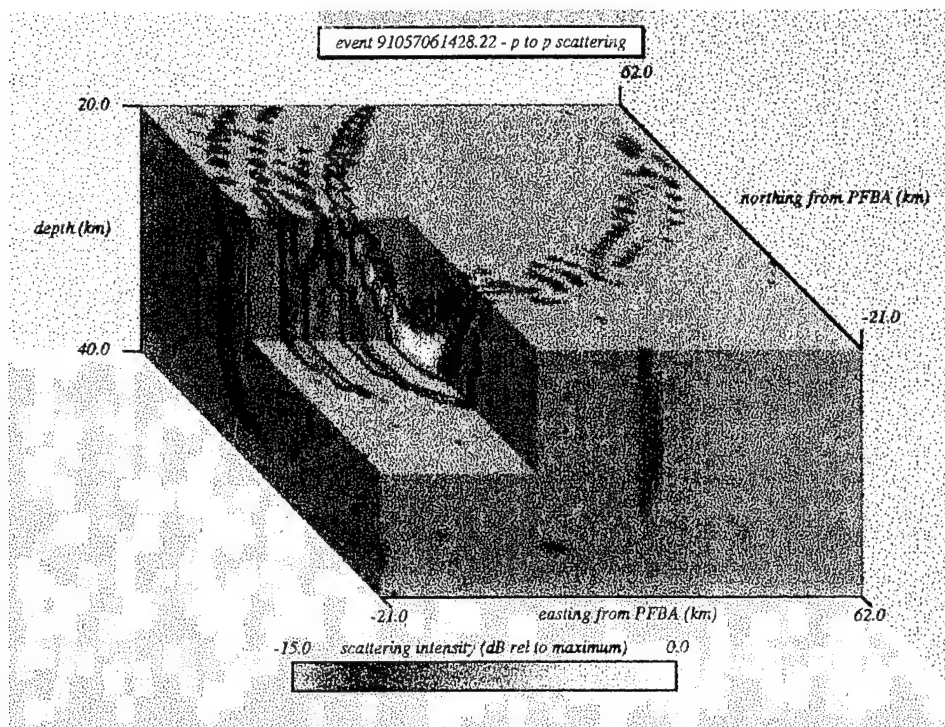


Figure 6: Three dimensional image calculated using event 91057061428.22. Note the distribution of energy in space along the 2.25 s isotime curve. The beaded nature of the energy distribution is an artifact of the gridding end with and is not due to sidelobes in the Impulse Response.

we expect energy resulting from *P-P* scattering in this plane should have. This figure allows us to predict where in the plane the scatterer should lie - at the intersection of the dashed curves in the upper and lower figures. At the bottom of Figure 5 we display an image of scattering intensity calculated from this event using the 19 available 3-C stations. The energy lies close to the 2.25 s curve and despite the imperfect slowness-resolution it is clear that an isolated source exists at roughly 30 km depth and roughly 20 km to the NNE of the array. In Figure 6 we display a 3-D image of the crust beneath the array obtained with our 3C migration technique. The image extends from 21 km south and west of the array to 62 km north and east between a depth of 20 to 40 km and is constructed from 41 x 41 x 31 grid points (in x,y and z). The corner has been removed to reveal the concentration of energy at 30 km depth. In this figure the effect of the limited resolution is indicated by the smearing of energy along the ellipsoidal surface. The beading is an artifact of gridding associated with the calculation of the image. The proximity of this feature to the San Andreas fault is intriguing (it is just south of the point of intersection with the Landers fault zone). The depth is puzzling, however, since at 30 km it is well below the seismogenic zone.

5. DISCUSSION

Since the rays involved cross a complicated crust (which includes the Coachella valley) there are a number of possible explanations. For example the late arrival might be a deeply penetrating, normally refracted, ray that has passed under the trough. It is possible that the late phase is not due to normal refraction but has been caused by scattering from a deeply buried feature at the northwestern end of the valley. Considering that a scattering process is unlikely to yield such a high amplitude arrival it seems

most likely that this phase has resulted from a bounce from a continuous interface. At a depth of 30 km this feature lies at the depth of the Moho (*Hadley & Kanamori, 1977*). The amplitude is suggestive of a near-critical angle reflection from the Moho, it is hard to imagine any scattering process that will yield that much energy. The fact that the phase is often absent, and when present often arrives from a biased direction, requires that the phase is not due to a simple bounce from a flat Moho. Although the velocity model we have used for the raytracing is 1-dimensional there is clearly a third dimension to the velocity structure and it seems most likely that the phase is bouncing from a highly contorted Moho. Although PFO lies on a stable, Mesozoic age, granitic batholith the larger region is tectonically active - as evidenced by the topography displayed in Figure 1. The Moho discontinuity does not likely approximate a horizontal plane but is likely contorted. The feature we have identified lies just south of the San Andreas fault zone at the northern end of the Coachella Valley. Although no study has clearly indicated the orientation of the Moho surface in this area it is widely believed (e.g. *Sung & Jackson, 1992; Zhao, Kanamori & Humphrey, 1994; Baker et al., 1995*) that the Moho tilts down to the northwest in this area as leaves the Salton trough. The regional tilt inferred from these studies is inconsistent with the tilt necessary for Moho bounces to be directed toward PFO from events to the northeast. *Jachens & Griscom (1985)* mapped isostatic gravity residuals assuming Airy compensation at the Moho and found no significant residuals. This indicates that crustal thickness can be inferred from free-surface topography - *i.e.* an inverse correlation should exist between topography on the Moho and at the free-surface. As shown in Figure 1 the topography drops sharply, from northeast to southwest, across the San Andreas fault north of the ANZA network as the transverse ranges contact the Salton Trough. The topography rises sharply just south of the trough in the vicinity of the network. If this topography is mirrored by topography on the Moho along the same profile the Moho would rise sharply at the San Andreas fault (assuming a density contrast at the Moho of 0.6 g/cc and a crustal density of 2.7 g/cc a 1000 m drop at the free-surface would correspond to a 4500 m rise in the Moho). A sharp rise in the Moho trending northwest-southeast is consistent with the topography that would be necessary to reflect energy arriving from the northeast toward PFO.

6. CONCLUSIONS

This project was initiated with the goal of identifying prominent, buried, scatterers that give rise to identifiable coda phases that might be confused with near source phases (*e.g.* those used to constrain depth). We have observed extreme variability in seismic coda recorded at local and regional ranges by ANZA and the PFBA in southern California. We believe that the variability is not solely due to scattering from volume heterogeneities but to the interaction of seismic energy with Moho topography. This work suggests that any analysis of event location that involves interface bounce phases (particularly those occurring in tectonically active areas) should consider the possibility of bias in the arrival direction and arrival time. Although this study has been used to describe and demonstrate the imaging technique these results do not represent a comprehensive search for heterogeneities in the vicinity of Piñon Flat.

7. ACKNOWLEDGMENTS

We benefited greatly from database and graphics software written by the JSPC group in Colorado.

8. REFERENCES

- Aki, K., 1969, Analysis of seismic coda of local earthquakes as scattered waves, *Journal of Geophysical Research*, 74, 615-631.
- Aki, K. & Chouet, B., 1975, Origin of coda waves: source, attenuation, and scattering effects, *Journal of Geophysical Research*, 80, 3322-3342.
- Baker, G.E. & Minster, J.B., 1995, PFO receiver function study, accepted *Journal of Geophysical Research*.
- Bannister, S.C., Husebye, E.S. & Ruud, B.O., 1990, Teleseismic P coda analyzed by three-component and array techniques: Deterministic location of topographic P-to-Rg scattering near the NORESS array, *Bulletin of the Seismological Society of America*, 80B, 1969-1986.
- Gupta, I.N., Lynnes, C.S., McElfresh, T.W. & Wagner, R.A., 1990, F-K analysis of NORESS array and single station data to identify sources of near-receiver and near-source scattering, *Bulletin of the Seismological Society of America*, 80B, 2227-2241.
- Gupta, I.N., Lynnes, C.S. & Wagner, R.A., 1990, Broadband F-K analysis of array data to identify sources of local scattering, *Geophysical Research Letters*, 17, 183-186.
- Hadley, D. & Kanamori, H., 1977, Seismic structure of the Transverse Ranges, California, *Geological Society of America Bulletin*, 88, 1469-1478.
- Hedlin, M.A.H., 1991, Analysis of seismic coda to identify regional sources and image strong crustal scatterers, Ph.D. thesis, University of California, San Diego.
- Hedlin, M.A.H., Minster, J.B. & Orcutt, J.A., 1991, Beam-stack imaging using a small-aperture array, *Geophysical Research Letters*, 18, 1771-1774.
- Hedlin, M.A.H., Minster, J.B. & Orcutt, J.A., 1994, Resolution of prominent crustal scatterers near the NORESS small aperture array, *Geophysical Journal International*, 119, 101-115.
- Hedlin, M.A.H. & Vernon, F.L., 1995, Site Characterization using a small aperture array, ms in preparation for submission to the *Geophysical Journal International*.
- Jachens, R.C. & Griscom, A., 1985, An isostatic residual gravity map of California. In: *The utility of regional gravity and magnetic anomaly maps*, E. W.J. Hinze, SEG, Tulsa, OK, 347-360.
- Key, F.A., 1967, Signal-generated noise recorded at the Eskdalemuir seismometer array station, *Bulletin of the Seismological Society of America*, 57, 27-37.
- Key, F.A., 1968, Some observations and analysis of signal generated noise, *Geophysical Journal of the Royal Astronomical Society*, 15, 377-392.

Lay, T., 1987, Analysis of near-source contributions to early P-wave coda for underground explosions. III. Inversion for isotropic Scatterers, Bulletin of the Seismological Society of America, 77, 1767-1783.

Lynnes, C.S. & Lay, T., 1989, Inversion of P coda for isotropic scatterers at the Yucca Flat test site, Bulletin of the Seismological Society of America, 79, 790-804.

Revenaugh, J., The contribution of topographic scattering to teleseismic coda in Southern California, Geophysical Research Letters, 22, 543-546.

Sung, L. & Jackson, D.D., Crustal and Uppermost Mantle Structure Under southern California, Bulletin of the Seismological Society of America, 82, 934-961.

Yilmaz, O., 1987, Seismic data processing, Society of Exploration Geophysicists, investigations in geophysics, volume 2.

Zhao, D., Kanamori, H. & Humphrey, 1994, Simultaneous inversion of local and teleseismic data for the crust and mantle structure of Southern California, 1994 SCEC Annual Meeting, Temecula, CA, Sept 23-25.

Empirical Characterization of Regional Seismic Coda - Constraining Depth

1. INTRODUCTION

We use network recordings of local aftershocks to empirically characterize local crustal wave propagation and look for robust coda phases that are dependent on source depth. These empirical results form the basis for a technique for constraining source depth in seismically active areas.

To search for robust depth phases we group aftershocks into bins dependent on “known” event depth and the range to the recording station. Considering each bin individually we stack the recordings after converting each trace to an envelope and aligning all traces on the first arrival. By repeating this procedure for a vertical set of bins we construct an “event column”. Using ANZA network recordings of Landers and Superstition Hills aftershock sequences we have constructed vertical component event columns at ranges from 0.6 to 1.1° spanning depths from the free surface to 10 km. In the resulting displays, which show the dependence of de-phased coda on range and depth, we see clear evidence of *PmP* (at ranges from 0.7 to 1.1°) but no evidence of any free-surface bounces at any of these ranges. Although synthetics suggest that, at the ranges considered, *pPg* and *pPmP* should have very small amplitude (relative to *Pg* and *PmP*) it is surprising that no robust *sPg* and *sPmP* phases are evident.

In spite of the presence of only a single depth phase (which does not exhibit a rapid moveout with respect to *Pg*) we have attempted to use these “event columns” to constrain event depth. A single-station event depth is estimated by cross-correlating the recording of the event with the appropriate event column (after removing the trace being considered from the event column). The network depth estimate is obtained from a weighted average of all single-station depth estimates (with preference being given to those stations with the highest single-trace to master-trace cross-correlations). From an analysis of 43 Landers aftershocks we have found that the cross-correlations do not depend strongly on depth. The depth residuals (“known” depth - our depth estimate) have zero mean with a standard deviation of 2.5 km. This residual decreases as the number of stations used increases. With 7 stations “voting” the residuals have a standard deviation of 2.0 km. In areas where free-surface depth phases are robust we expect that this approach would yield smaller depth residuals.

2. SYNTHETIC AND RECORDED DATA

2.1 Wavenumber Integration

In this section we use Wavenumber Integration (WI - *Apsel and Luco, 1983; Luco and Apsel, 1983*) to synthesize local and regional waveforms.

2.2 ANZA network recordings

We have examined local recordings of seismic events in southern California made by the ANZA network. The ANZA network made triggered and continuous mode recordings of the June 28 1992 Mw 7.3 Landers event and 158 aftershocks above M 4.0 (Figure 7). This linear aftershock trend gives us an opportunity to view the behavior of coda phases with range since the ANZA network stations recorded the events at ranges from 0.28 to 1.28° . The Mw 6.0 Superstition Hills main shock occurred in November, 1987 and was followed by 35 events above Ml 3.5. The vast majority of these events occurred within 10 km of the free-surface.

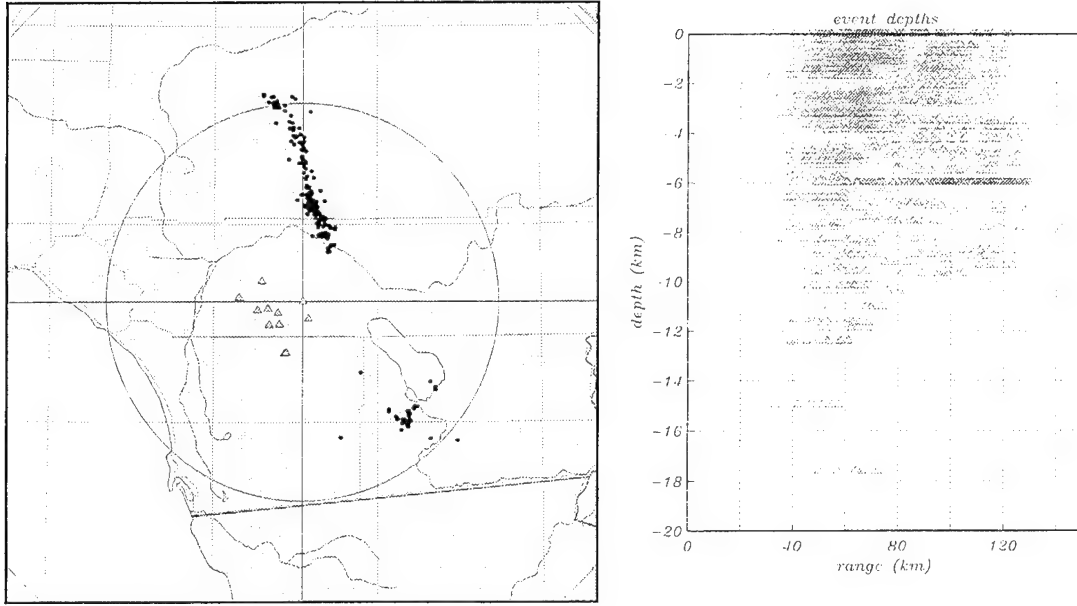


Figure 7: Landers and Superstition Hills aftershocks are shown on the left (with ANZA network stations represented by the triangles). On the right are the two aftershock sequences in range and depth..

3. PRELIMINARY ANALYSIS

Prior to an analysis of recorded data we have considered used WI to predict the response of the southern California crustal model (Zhao & Helmberger, 1994) to various dislocation and dilatational sources. We have calculated a suite of synthetics using WI for dislocation sources ranging from 0.5 to 9.5 km deep at a range of 1° (Figure 8). The focal mechanism used was that of a vertical right-lateral strike slip dislocation on trend with the Landers aftershock sequence recorded at the site of station PFO in ANZA. In this figure we display travel times for Pg , pPg , sPg , $pPmP$ and $sPmP$ and find that the pPg and $pPmP$ phases are not discernible. At this range we expect little energy in the “little P” phases (due to inefficient conversion of upgoing compressional energy at the free surface). These dislocation sources generate enough shear wave energy to yield significant sPg and $sPmP$ - these phases are comparable in amplitude to Pg and PmP - in addition to a number of higher order crustal resonance phases. The “little S” phases are potentially very useful for depth determination because they move out rapidly with respect to Pg .

4. EVENT COLUMNS

By binning and stacking event recordings (after aligning on the P onset and converting the traces to envelopes) we can empirically characterize crustal wave propagation and look for coda variations with event depth and source-receiver range. We expect some loss in temporal resolution will result from

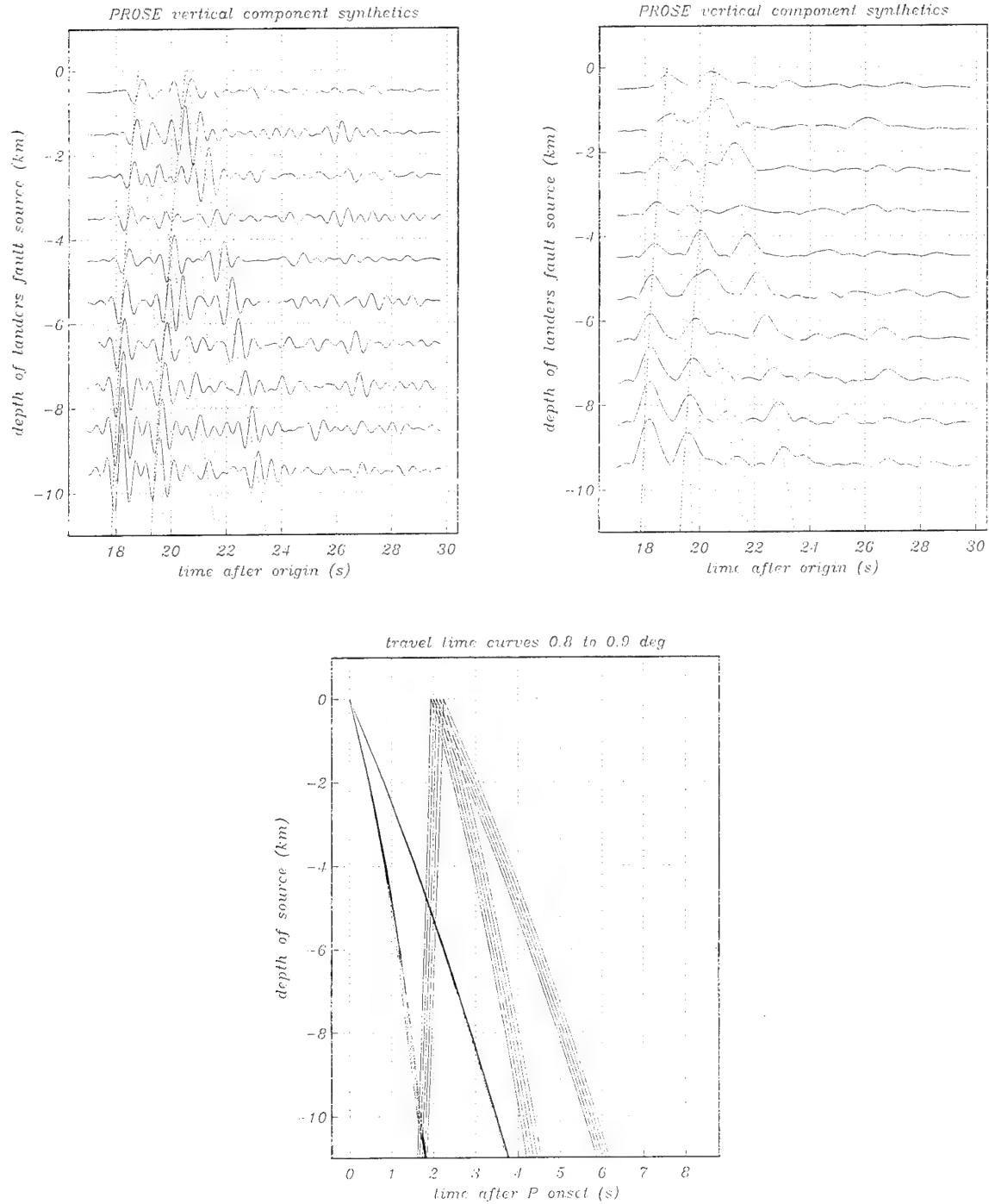


Figure 8: On the upper left we show a vertical suite of WI earthquake synthetics. Superimposed on the synthetics are travel time curves for pP , sP , $pPmP$ and $sPmP$. On the upper right we show the same traces after conversion to envelopes. On the bottom we show the travel time curves resulting from binning sources in range from 0.8 to 0.9°. The binning has the most significant affect on the PmP phases.

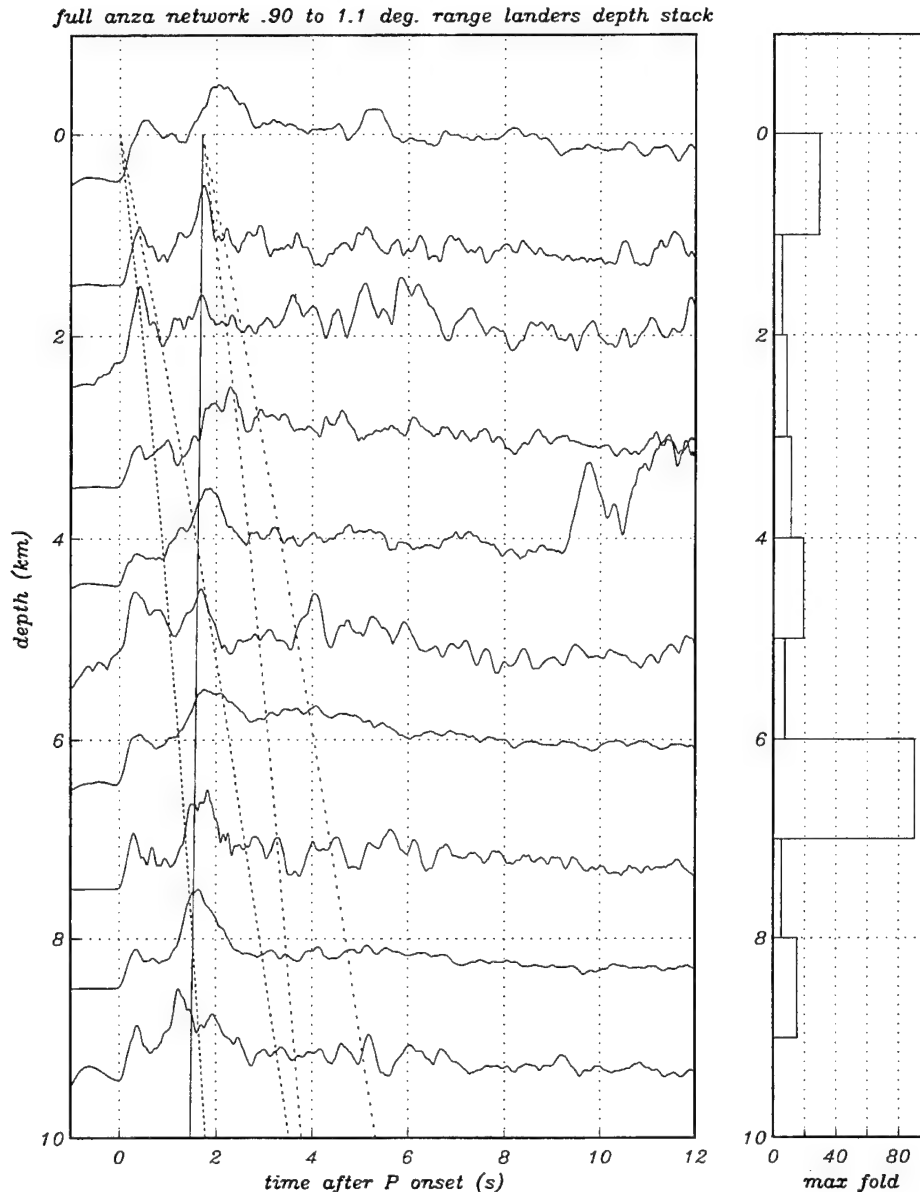


Figure 9: An event column based on Landers aftershocks occurring 0.9 to 1.1° from the station. Superimposed on this figure are travel time curves for pP , sP , $pPmP$ and $sPmP$. To the right is a histogram indicating the number of recordings in each bin.

converting to envelopes and binning (Figure 8). The binning should have the greatest effect on the PmP phases.

Actual event columns are shown in Figures 9 to 11. The first and second were calculated using Landers aftershocks from 0.9 to 1.1° and from 0.8 to 0.9° . The third column used aftershocks to the Superstition Hills mainshock. Each column is paired with a histogram showing the number of events that were used in each bin. The concentration of events at 6 km in Figures 19 and 20 is not physical but an artifact of the software package used to make the original depth estimates. These events have been excluded from further consideration.

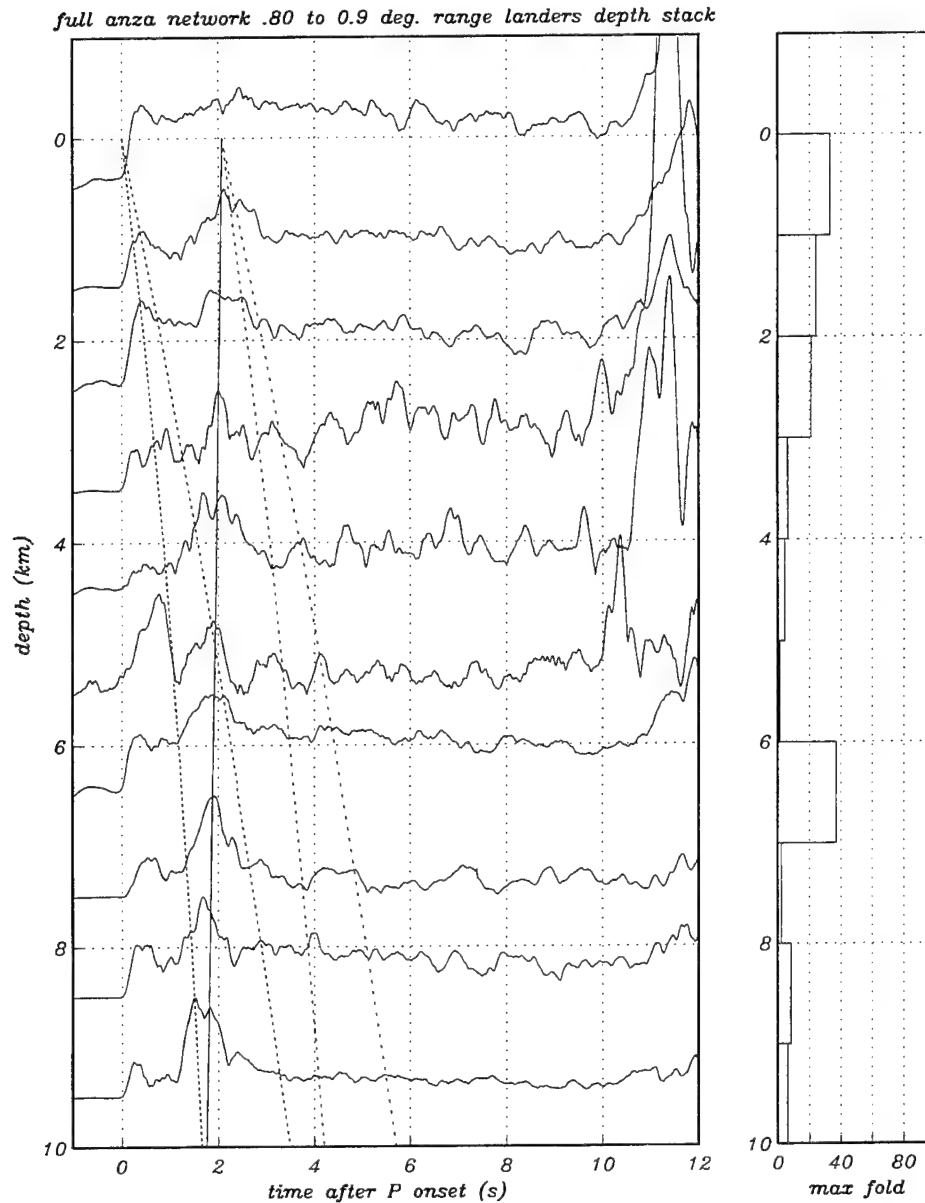


Figure 10: This figure is the same as Figure 9 except it uses Landers after-shocks located 0.8 to 0.9° from the station.

We clearly see a *PmP* phase in all the event columns. In the Superstition Hills event column this phase arrives significantly earlier and suggests a thinner crust (30 vs 35 km). There is no evidence in any of these event columns of any free-surface bounce phases (incl. *pP* as expected, and *sP* phases).

5. DEPTH ESTIMATION

In spite of the absence of numerous robust coda depth phases, and the fact that the one that is present, *PmP*, shows little move-out with respect to *Pg*, we have attempted to use these event columns to esti-

full anza network 0.8 to 0.9 deg. range superstition hills depth stack

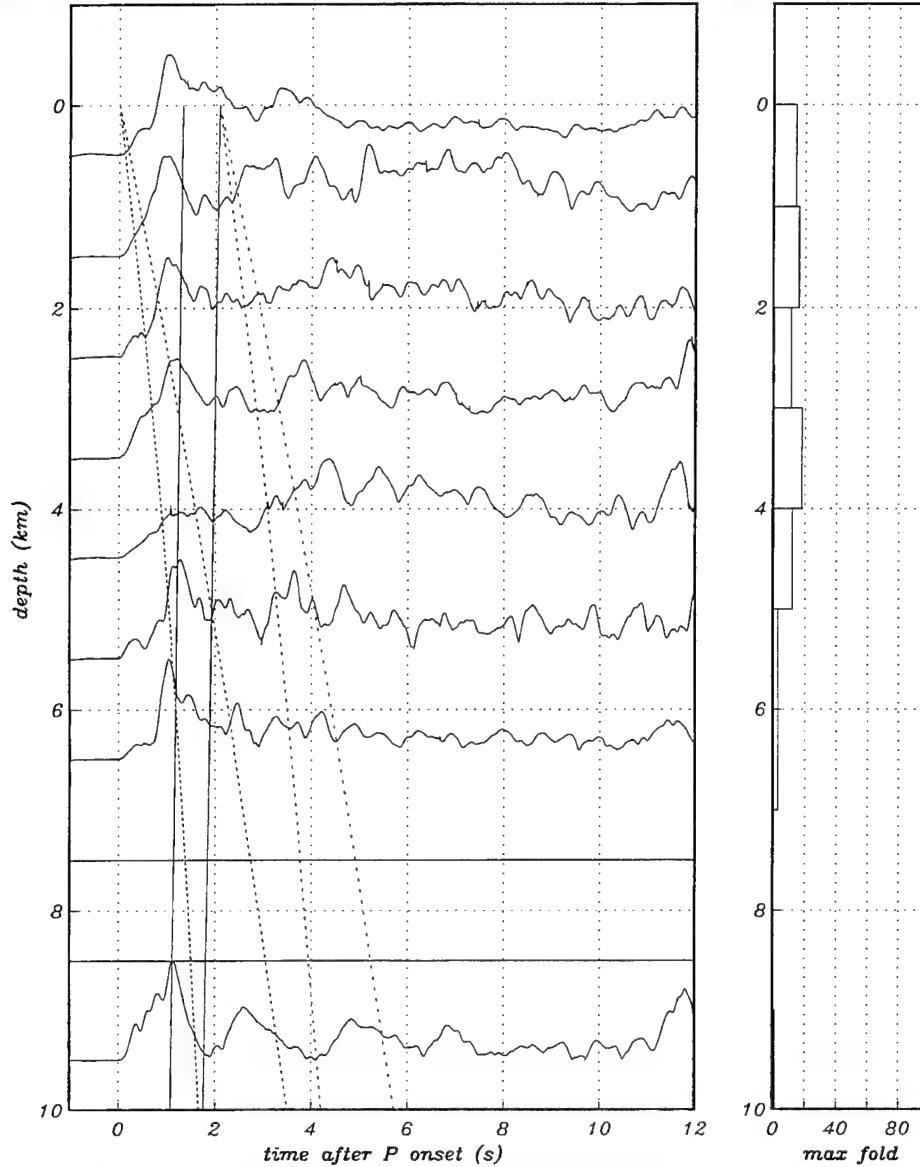


Figure 11: This figure is the same as Figure 9 except it uses Superstition Hills aftershocks located 0.8 to 0.9° from the station.

mate the depths of these events. The scheme we have adopted is simply based on the cross correlation between a single-station recording of an event and all master-traces in the event column at the source-receiver range. In principle, given a vertically varying suite of master-traces, this cross correlation should be greatest at the actual event depth. One advantage of this approach is that it depends on phases being present in coda but it is not necessary that these phases are identified or modeled - it is simply based on the shape of the envelope of the entire waveform. It is assumed that the event range is constrained well enough to allow comparison with the correct event column.

As an example of this approach we show, in Figure 12, single- to master-trace cross correlations as a function of the residual between the known event depth and depth of the master-trace (known - our

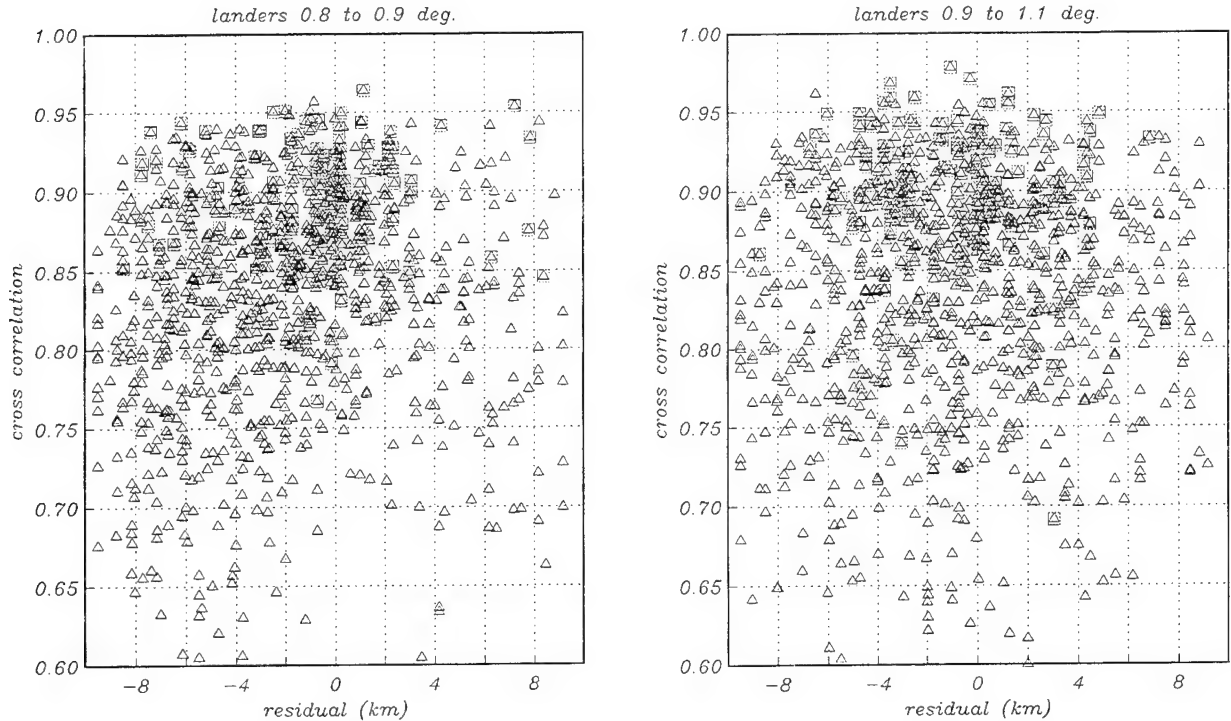


Figure 12: All single- to master-trace cross correlations are shown here (for the event columns shown in Figures 9 and 10) and are represented by the triangles. The squares represent the best single-station cross-correlations (i.e. the single-station depth solutions). These solutions cluster around a zero residual.

depth) for events located in the Landers aftershock sequence between 0.8 and 0.9° . The single-station solutions (the depths at which the cross-correlation was greatest) are represented by the boxes and are clearly clustered about a zero residual. The mean of the solutions is -0.89 km with a standard deviation of 3.3 km. The standard deviation of the residuals is directly dependent on the rate at which the cross-correlations change with depth. Due to the absence of any coda phases with rapid moveout with respect to Pg this variation is subtle. Considering Landers aftershocks from 0.9 to 1.1° from the station (Figure 12 right side) the result is essentially the same.

By considering all network recordings of an event simultaneously the depth residuals can be decreased. By simply forming a weighted average depth estimate (with weights given by the single- to master-trace cross correlations) we find that the depth residuals decrease with increasing numbers of stations (Figure 13). With 7 stations voting the standard deviation is 2.0 km. With two stations reporting the residual is 3.46 km. The standard deviation for all events located with multiple stations is 2.5 km.

6. CONCLUSIONS

An empirical technique for characterizing local and regional event coda, like the one described above, might be useful in seismically active areas where the possibility of clandestine testing exists. It might be sufficient to characterize the coda using a temporary deployment, and then using a smaller scale, more permanent, local or regional network to monitor seismicity and contribute time-series for comparison to the master-traces. Unless monitoring occurs in an area in which robust free-surface phases are

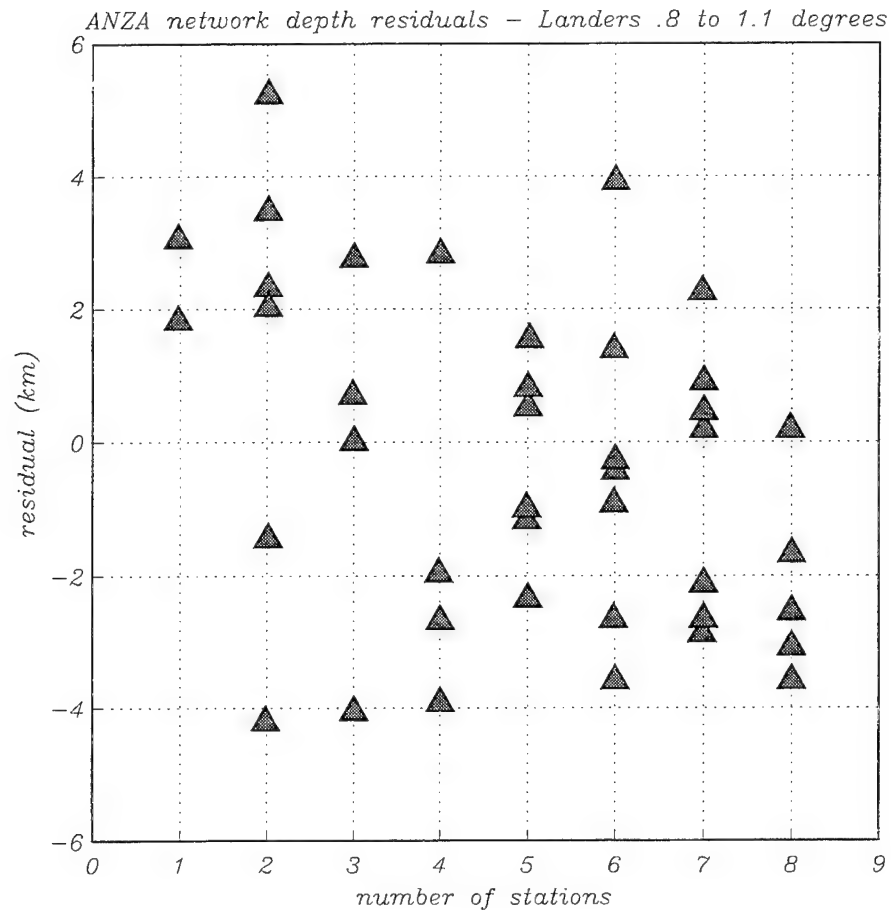


Figure 13: ANZA network depth residuals obtained using the event columns displayed in Figures 9 and 10.

present then a significant (~10) number of stations might be necessary to yield the necessary depth resolution to distinguish deep earthquakes from events shallow enough to possibly be nuclear tests.

7. REFERENCES

Apsel, R.J. & Luco, J.E., 1983, On the Green's functions for a layered half-space, part II, Bulletin of the Seismological Society of America, 73, 931-951.

Luco, J.E., & Apsel, R.J., 1983, On the Green's functions for a layered half-space, part I, Bulletin of the Seismological Society of America, 73, 909-929.

Zhau, L-S & Helmberger, D.V., 1994, Source estimation from broadband regional seismograms, *Bull. Seismol. Soc. Am.*, **84**, 91-104.

A new time-frequency discriminant based on similarity

1. INTRODUCTION

Under previous Air Force contracts we developed a discriminant that seeks long-lived spectral modulations in the major phases and coda. Long lived modulations can be produced by seismic resonance and by ripple firing and hence, given a non-resonant crust, can be diagnostic of ripple-fired events. In order to aid automated recognition *Hedlin et al (1989)* developed a procedure in which a binary sonogram is derived from the original, spectral, sonogram by the application of filters which replace local spectral information with a binary code which simply reflects local spectral highs and lows. The binary conversion is achieved by convolving each spectral estimate within the sonogram with two boxcar functions to yield two smoothed versions of the spectrum - one heavily smoothed and the other relatively unsmoothed. The binary sonogram simply results from the difference between the two sonograms with local highs and lows represented by ± 1 respectively.

In Figure 15 we show sonograms calculated from regional observations of a single-explosion (top) and a quarry blast (bottom) recorded by the NRDC network in Kazakhstan (Figure 14). The corresponding binary sonograms are shown in Figure 16 (top row). On the bottom row we show binary sonograms calculated from the North-South and East-West recordings of the quarry blast. These binary sonograms show a remarkable independence of the energy from the recording component and from time. Previously we examined the time-independence as a discriminant (*Hedlin et al., 1989; Hedlin et al., 1990*). In this section we will determine if the independence from the recording component might also be useful as a discriminant.

2. DATASETS

For this section we have chosen to analyze two datasets collected in central Asia. The NRDC network (Figure 14) was deployed in 1987 in central Kazakhstan and collected triggered 250 sps recordings at the surface and in boreholes of three calibration explosions, numerous local and regional quarry blasts and a large number of far-regional/teleseismic earthquakes.

The 10-station telemetered KNET was deployed in Kyrgyzstan in 1991 (Figure 14). Located within an aperture of 200 km between the Kazakh platform to the north and the Tien Shan to the south, this network is ideal for recording and studying events along the seismically active southern flank of Eurasia. The network has made 100 sps triggered and 20 sps continuous mode recordings of quarry blasts and earthquakes and local and regional distances in addition to recording a large number of teleseisms.

2.1 A priori event ID:

Given that we have not had access to "ground-truth" information, which would positively identify the type of each event analyzed, we have relied on various non-seismic sources of information. Identification of the non-calibration events in the seismically quiet Kazakh platform were provided by Cliff Thurber who used SPOT photos to confirm mining activity at event locations. We have found no descriptions of shooting technique at these locations. Event identification in Kyrgyzstan was somewhat more difficult. With a hand-held GPS unit Rob Mellors identified an area northeast of station CHM which contained a large limestone quarry (43.028 N, 74.888 E) with shots typically occurring in

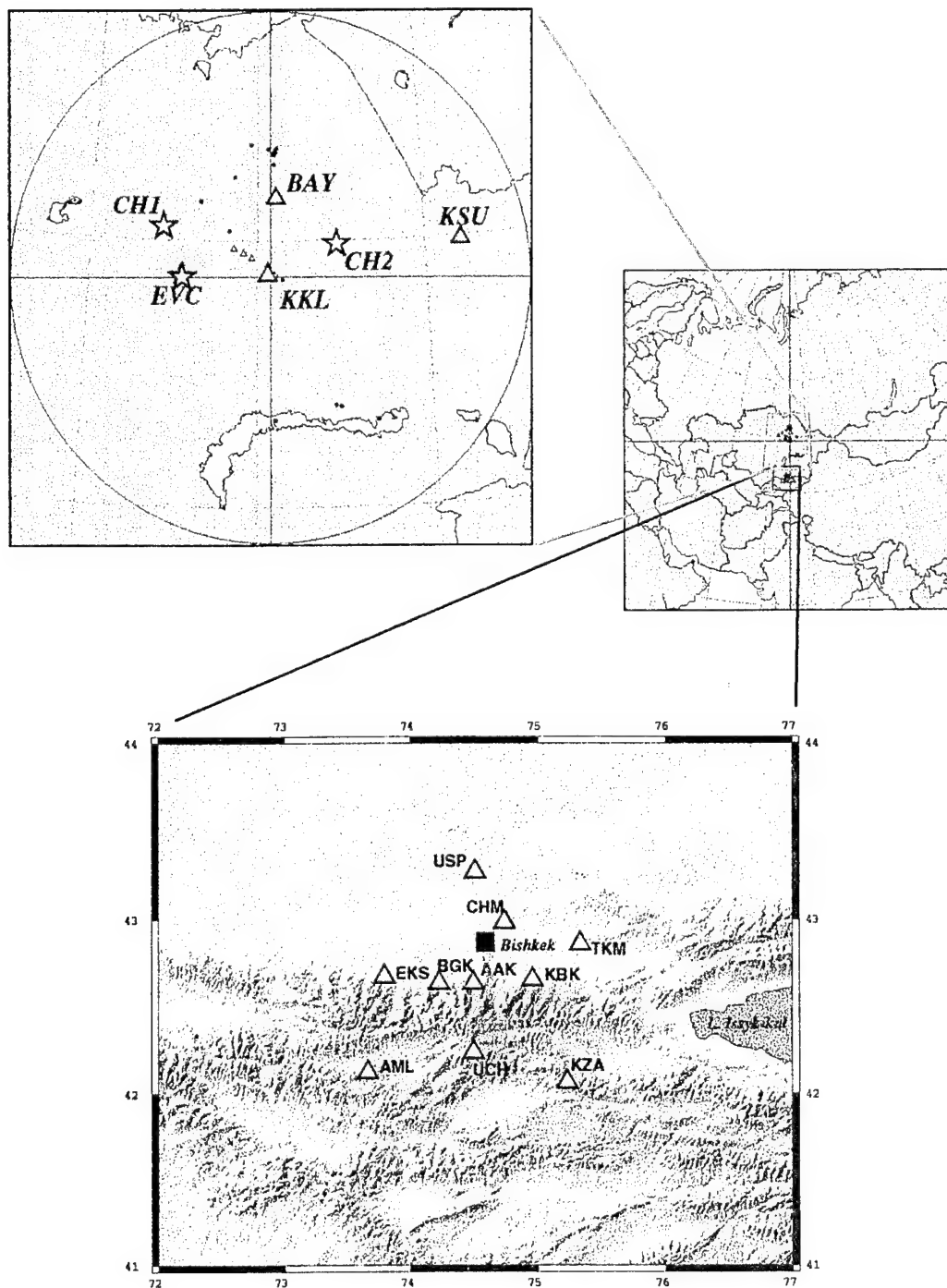


Figure 14: The NRDC and KNET deployments. The NRDC figure shows event locations. The highlighted events include CH1 and CH2 (the calibration explosions) and EVC (a quarry blast).

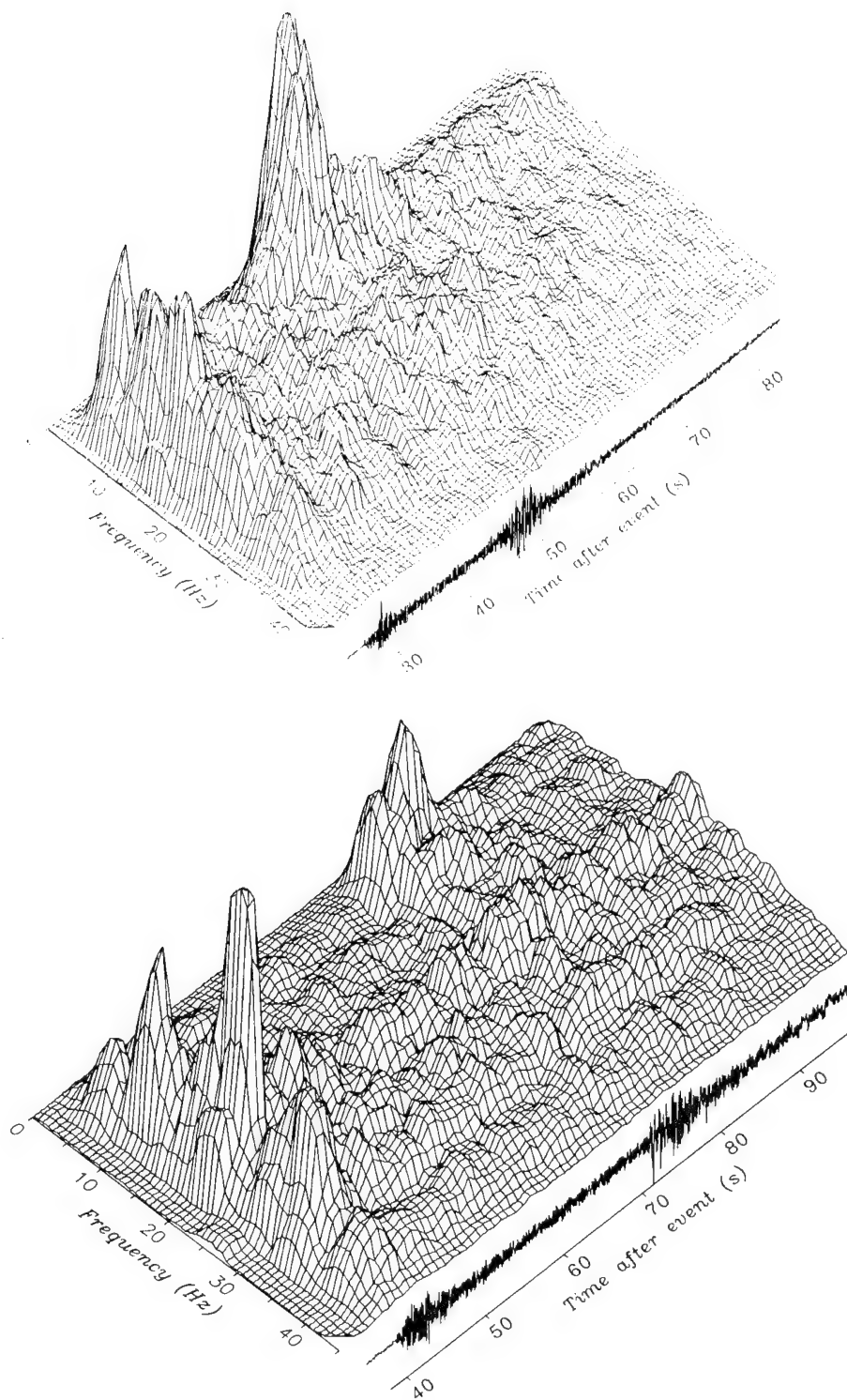


Figure 15: Two sonograms (with time-series) calculated using NRDC recordings. On the top is the sonogram of CH2 recorded at Bayanaul. On the bottom is the sonogram of EVC also recorded at Bayanaul.

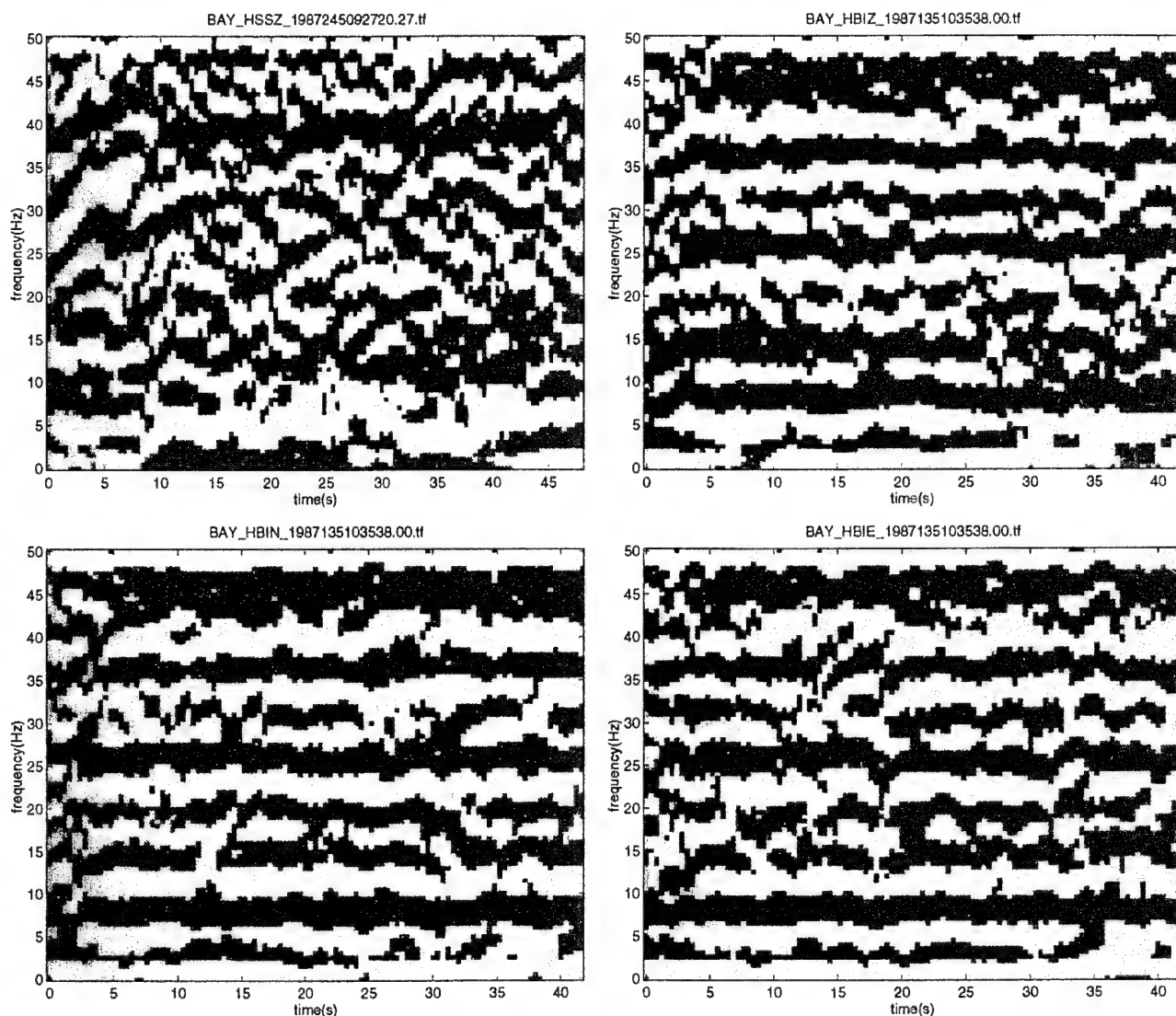


Figure 16: Four binary sonograms calculated using NRDC recordings. On the top row are binary sonograms calculated using the recordings displayed in Figure 15. CH2 is on the left, EVC is on the right. On the bottom row are binary sonograms of EVC calculated using the N-S and E-W Bayanaul recordings.

the late afternoon. Recordings of some of these events made at CHM contain obvious air blasts roughly 37 s after the P onset.

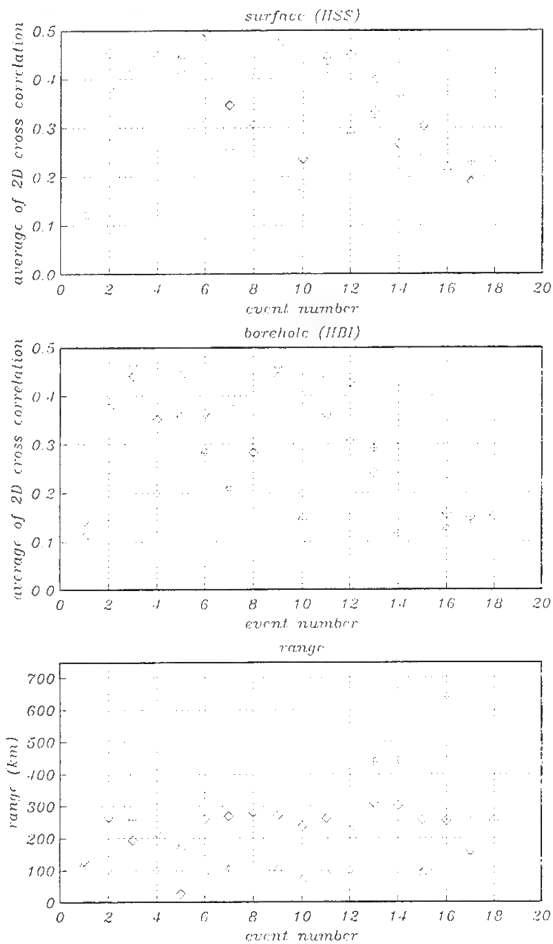
3. ANALYSIS OF KNET AND NRDC DATA

As we noted in section 1 ripple fired events are capable of generating coda that is remarkably independent of the recording direction. In this section we attempt to determine if this trait can be used to distinguish these events from earthquakes and explosions. Using KNET and NRDC we consider discrimination with single stations and full networks.

The procedure that we have developed to quantify the independence of the time-frequency patterns from the recording direction is based on a zero-lag cross-correlation. In Figures 17 to 21 we display the

NRDC

Single station



Network

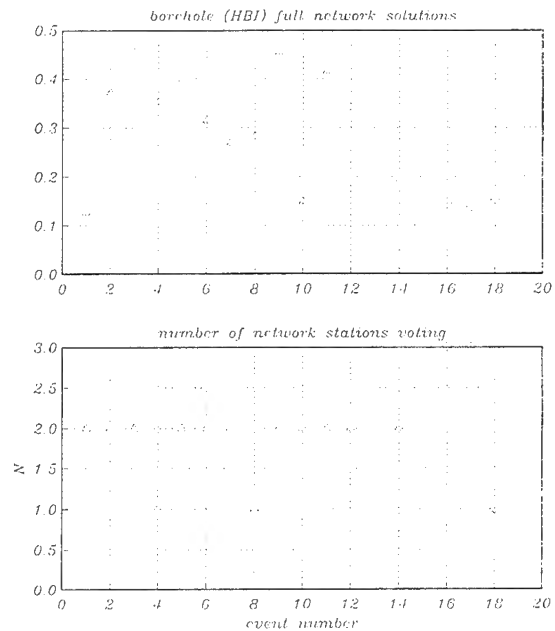


Figure 17: The results of applying the similarity discriminant to the NRDC dataset. In this figure events 1 to 15 are believed to be quarry blasts, 16 to 18 are the calibration explosions. On the left we show single station solutions, the full network solutions (using the borehole high-gain channel) are shown on the upper right (with the number of stations displayed below).

average of a three-way cross-correlation between each pair of recording channels (*i.e.* Z v E-W/ Z v N-S & N-S v E-W).

3.1 NRDC:

Considering single-station solutions the borehole sensors yield a better separation, the surface station at KSU is resonant (Figure 17) and thus has a high degree of similarity between the recording directions. Considering borehole recordings the calibration explosions are tightly grouped. There are clearly two outliers among the quarry blasts (events 1 and 10) which are discussed below. The network solu-

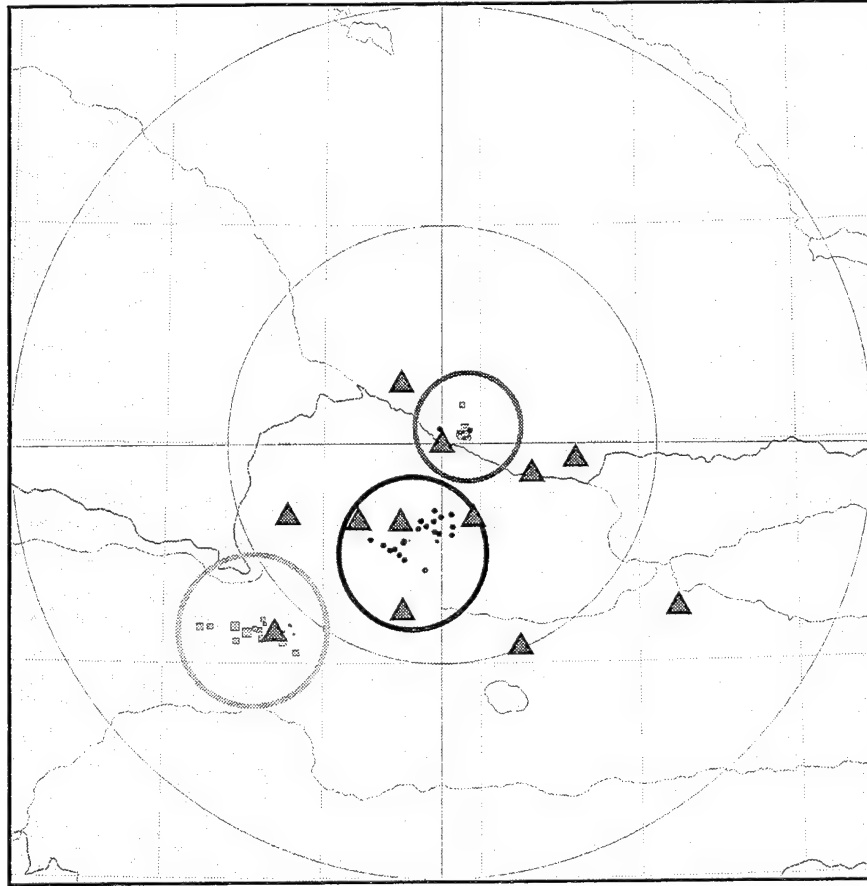


Figure 18: The KNET and the events used in Figures 19 to 21. The three circles represent the three event populations. The upper right circle encloses the limestone quarry location that gave rise to the 50 quarry blasts used in the calibration and testing of the similarity discriminant. In the circle on the lower left are the earthquakes (aftershocks to the Mw 7.4 Suusamyr thrust earthquake) used in calibrating the discriminant in this area. The middle circle encloses the earthquakes that were used to test the discriminant.

tions (calculated by forming a weighted average of the single station solutions with weighting to give preference to sonograms with higher SNR) appear to be slightly more robust (although generally only 2 stations voted so the difference is slight).

3.2 KNET:

In this dataset (Figures 16 and 18) there are enough events to permit calibration of the discriminant and testing on an independent dataset. The calibration of the discriminant, using quarry blasts north of CHM and earthquakes to the south of AML (aftershocks to the Mw 7.4 Suusamyr thrust earthquake), shows that single-station solutions are highly scattered (Figure 19). Calculating network solutions we find that the earthquake population is tightly grouped and little crossover with the quarry blasts exists (Figure 20). Shown in this figure are the mean and $\pm 1, 2$ and 3 standard deviations.

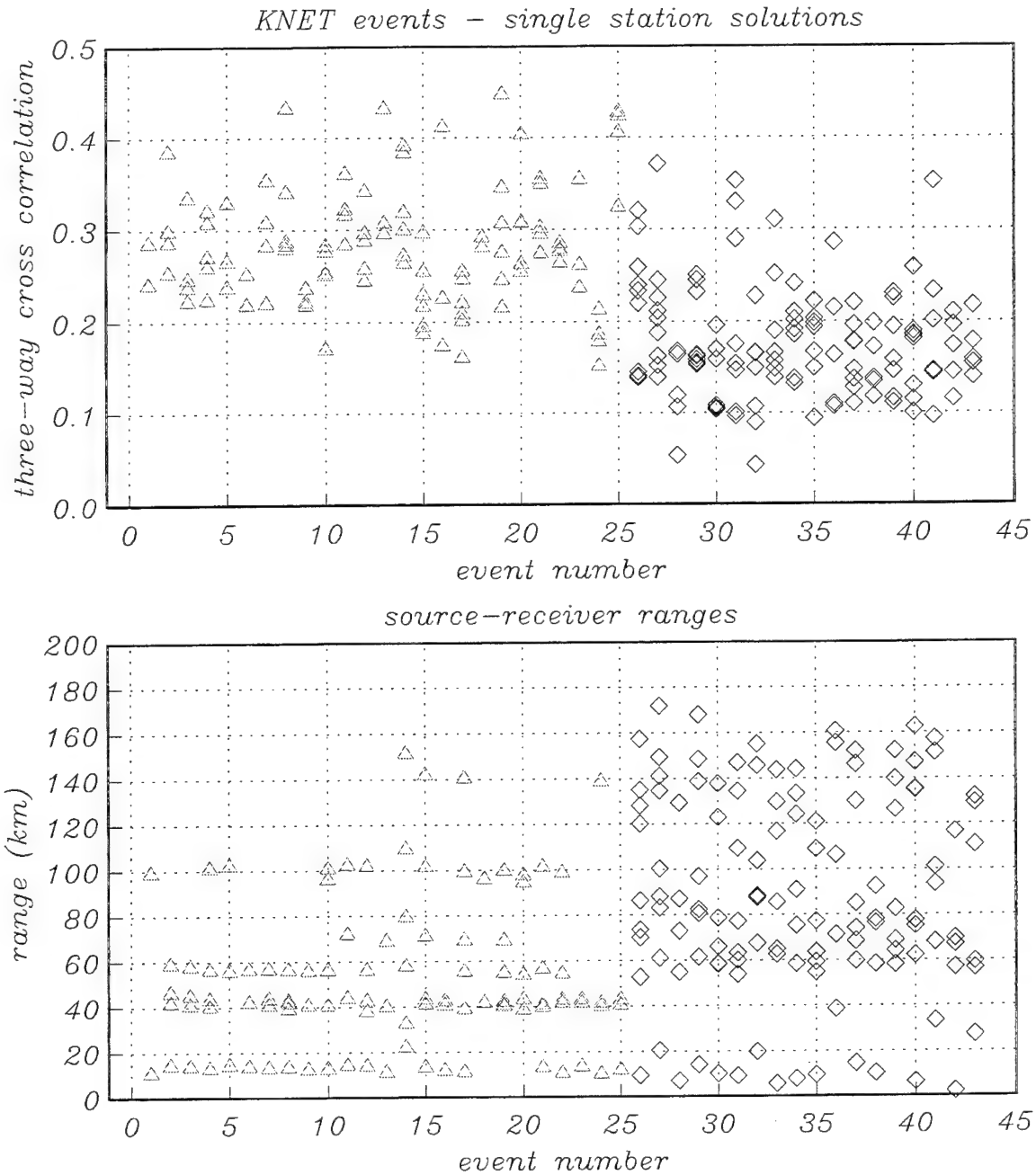


Figure 19: Single station solutions and ranges. Events 1 to 25 are believed to be quarry blasts. The remaining events are aftershocks to the Suusamyр thrust event.

Using earthquakes located near station AAK, and different quarry blasts from the same mine, we find that the network solutions are essentially the same (Figure 21). The standard deviation lines are from the calibration set of earthquakes (Figure 20). When a network is available the similarity discriminant appears to be quite effective and robust at local and near-regional ranges. This qualitative assessment will be followed shortly by a more rigorous description of population separation and misclassification probability based in statistics.

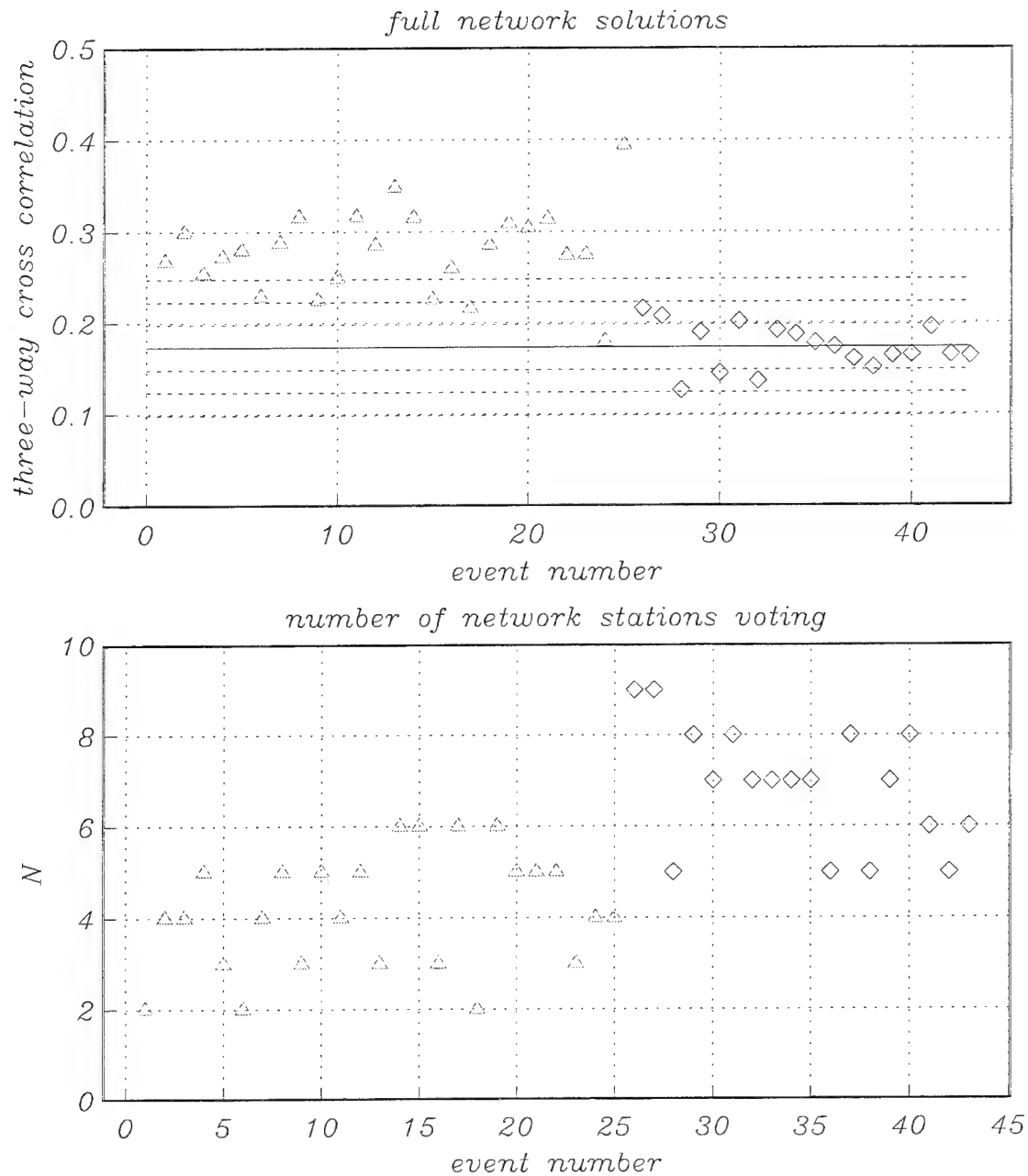


Figure 20: Network solutions using the same (calibration) events considered in the preceding figure. On the bottom we display the number of stations used in each solution. The earthquake solutions follow a normal distribution. The horizontal lines represent the mean and $\pm 1, 2$ and 3 standard deviations.

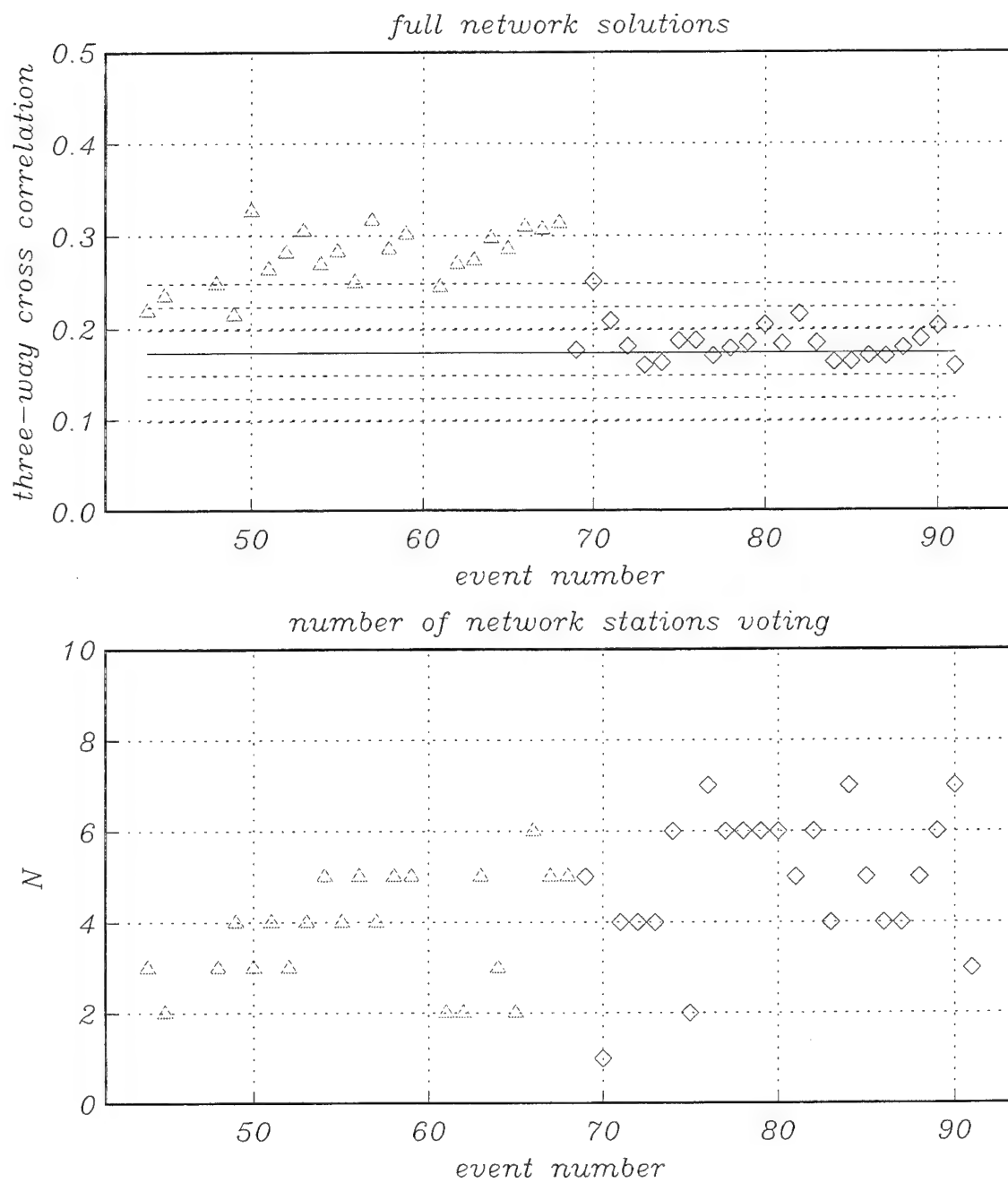


Figure 21: Network solutions using the test events (see Figure 20). The horizontal lines in the top figure are reproduced from Figure 22 (the calibration events).

3.3 Outliers

An important aspect of our research program is exploring the reasons for outliers. In section 3 the similarity discriminant produced several outliers. In this section we consider three of them. Some outliers can be explained as the result of poor station coverage (e.g. KNET event 70 which was recorded by a single station). Other outliers were recorded by more than 1 station (e.g. NRDC events 1 & 10 - 2 stations and KNET event 26 - 9 stations). Unless our a priori event ID's are incorrect the similarity algorithm judged the NRDC quarry blast to be an explosion and the KNET earthquake to be a quarry blast.

NRDC events 1 & 10, believed to be quarry blasts, appear to have generated no spectral modulation in the band from 0 to 50 Hz. There are a number of possible explanations - the delays chosen were so short that no modulations were observed below 50 Hz. In theory this could be caused by delays < 20 ms however even with such delays we might expect modulations caused by source finiteness. Another alternative is that due to shot scatter or to the spatial configuration of the shots there was not enough shot regularity to produce modulations at any frequency. It is also possible that these events were not quarry blasts but were earthquakes, due to natural forces or related to the mining activity. Unfortunately without "ground truth" information we can only speculate as to the cause of these outliers.

KNET event 26 is believed to be an earthquake that appears to have a significant amount of time-independent energy. This could be caused by near-source resonance however, given that all earthquakes in the group used to calibrate the discriminant are tightly grouped, it is odd that the other events were not similarly affected.

4. CONCLUSIONS AND FUTURE PLANS

4.1 Conclusions:

It appears that similarity can be used to separate quarry blasts from instantaneous explosions and earthquakes. When used to discriminate between earthquakes and explosions in Kyrgyzstan the similarity discriminant is much more robust when a network is available. In Kazakhstan the probability of misclassifying an instantaneous explosion as a mining event is higher when surface stations are used - probably because of near-surface resonance at some sites.

Outliers, present in both the KNET and NRDC analyses, cannot be properly explained without ground truth information. We need more controlled experiments involving quarry blasts and calibration explosions with ground truth information for all events.

4.2 Future Plans:

Although this result comes at the end of the contract period it is preliminary to the larger effort of developing effective means to discriminate ripple-fired events from instantaneous explosions and earthquakes. This will be continued under our current contract F19628-95-K-0012. We are currently creating a technique that merges the time-independence and component independence into a single discriminant.

In addition we need to extend this research by analyzing array and network recordings made in other regions at greater ranges to test robustness and transportability and determine the effective range of the discriminants. Wherever possible we will analyze ground truthed data to better understand outliers.

should be produced by mines that use short (e.g. 20 ms) delays especially when delay times are irregular. We will test the theory that source finiteness can yield a low frequency time-independent signature.

5. REFERENCES

Hedlin, M.A.H., Minster, J.B. & Orcutt, J.A., 1989, The time-frequency characteristics of quarry blasts and calibration explosions recorded in Kazakhstan, U.S.S.R., *Geophysical Journal International*, 99, 109-121.

Hedlin, M.A.H., Minster, J.B. & Orcutt, J.A., 1990, An automatic means to discriminate between earthquakes and quarry blasts, *Bull. seism. soc. Am.*, 80B, 2143-2160.

Appendix A. Sono

1. OVERVIEW

The purpose of the sonogram software is to expand time series into 2-dimensional displays which show the dependence of spectral energy on time and frequency. Our research into the time -frequency characteristics of single and multiple chemical explosions detonated and recorded in Kazakhstan, FSU (*Hedlin et al., 1989*) indicates that a time -independent spectral modulation can be caused by ripple -firing (a blasting technique in which a number of closely grouped explosions are detonated in rapid sequence).

The sonogram software expands a time series into a time -frequency display by using a multi -taper spectral estimation procedure. Successive spectral estimates are obtained from data isolated by a sliding window. Multi -taper spectral estimation has been used because of the proven ability of this approach to yield minimally biased spectral estimates from short time series. See *Park et al. (1987)* for an explanation of this technique.

Given the complex nature of most spectral estimates we have introduced the option to reduce the sonograms to *binary form*. In this processing each spectral estimate is converted into two smoothed versions which are sensitive to small - and large -scale spectral features. These versions are obtained by convolving the spectral estimate with a short and long boxcars respectively.

By differencing the two estimates and replacing the difference at each frequency with a **+1** to indicate locally high power and a **-1** to indicate the opposite we convert the original spectral estimate into a binary spectral estimate. Applying this, highly processing to each individual spectral estimate in the sonogram yields a two -dimensional binary pattern. In *Hedlin et al. (1989, 1990)* we found that this processing aided discrimination by suppressing minor spectral details and thus enhancing any time -independent spectral signature that might be present.

Given the density of seismic stations in some areas (due to regional networks or arrays) many seismic events are redundantly recorded. As a result it is possible to enhance the time -frequency spectral estimates by stacking. As discussed in *Hedlin et al. (1990)*, stacking can be performed in many ways (e.g. before or after conversion to binary form). It has not been proven which approach is best. As a result we have not included this capability in this version of the sonogram software. Stacking sonogram matrices is easily performed within matlab.

2. APPLICATION

In the figures following the man page we show an application of sono to events recorded by the NRDC network in Kazakhstan (Figure 1). In Figure 2 we show the time-series and sonogram of a calibration explosion (CH2 recorded at high gain by the vertical component surface sensor at Bayanaul). This sonogram displays no organization of energy into time-independent bands (as expected) since the source is an instantaneous explosion. The sonogram displayed in Figure 3 shows significant banding. This is believed to be the result of ripple firing at the source. In Figure 4 to 6 we schematically show the method by which we convert spectral sonograms to binary form. The intent of this conversion is to

suppress large scale features in the sonogram and enhance small-scale features (like time-independence) that might indicate ripple-firing.

3. REFERENCES

Hedlin, M.A.H., Minster, J.B. & Orcutt, J.A., 1989, The time-frequency characteristics of quarry blasts and calibration explosions recorded in Kazakhstan, U.S.S.R., *Geophysical Journal International*, 109-121.

Hedlin, M.A.H., Minster, J.B. & Orcutt, J.A., 1990, An automatic means to discriminate between earthquakes and quarry blasts, *Bull. Seismol. Soc. Am*, **80**, 2143-2160.

Park, J., Lindberg, C.R. & Vernon, F.L., 1987, Multitaper spectral analysis of high-frequency seismograms, *J. Geophys. Res.*, **92**, 12675-12684.

NAME

sono - calculates, indexes, and stores a sonogram (amplitudes in the time-frequency plane) for a seismogram.

SYNOPSIS

sono - returns the proper "usage line".

sono par=parfile

No spaces are allowed around "=" on the command file.

ENVIRONMENT

Sono is designed to operate in the CSS 3.0 database environment. The program was tested with both the ORACLE and SYBASE database management systems.

For users of the SYBASE DBMS, the following environment variables should be set: SYBASE, DSQUERY, GDIHOME. SYBASE and DSQUERY specify the interface with the DBMS, and GDIHOME is set to the top directory where the SAIC Generic Database Interface (GDI) is installed.

For example,

```
setenv SYBASE /data/sybase/sybase492
setenv DSQUERY SYBASE492
setenv PATH $SYBASE/bin:$PATH
setenv GDIHOME /data/db_libs/libgdi
```

For users of the ORACLE DBMS the following environment variables should be set ORACLE_HOME, ORACLE_SID.

For example,

```
setenv ORACLE_HOME /data/oracle/6036
setenv ORACLE_SID dev6036
setenv PATH $ORACLE_HOME/bin:$PATH
```

Users must have a valid account, password, and a default database to access and use. This database must consist at least of the wfdisc, lastid and tfdisc tables. See the section TFDISC TABLE below for a description of tfdisc.

INPUT

The input to **sono** follows the style developed at SAIC for the various waveform management and database access libraries. User input is specified through a "parameter file" *parfile* which contains an ASCII description of user-specifiable parameters. A *parfile* consists of a list of parameters and values of the form **parameter=value**, as required by the program. No spaces are allowed around "=" in the file. All parameter names should be spelled exactly as they appear below (see section PARAMETERS). All parameter values that are character strings are case-sensitive unless noted otherwise.

Parameters can appear in any order. If any parameter needed for proper execution is missing, then the program exits with an error message informing the user of the missing information. Comments are allowed anywhere in the file, but not on the same line as a parameter. Comment should not start with a valid parameter name. For stylistic reasons, it is preferable to adopt a single convention for the comments syntax.

The parameters in the file can be divided into two sections according to their use by the program. The first section provides parameters for the database connection and access. The second section includes parameters which control the sonogram algorithm and calculation.

Example of *parfile* :

```
# The following line is just a comment
##### for DB connection #####
in_db=nrdc/nrdc
account="nrdc"
password="nrdc"
vendor="sybase"
# this is a comment line
sta_list="BAY"
chan_list="HSSE"
start_time=548073338.0
# if preferred, use end_time instead of
# duration, but not both
duration=35.0
extension_time=360
join=2
wfd_to_wfm

# The following line is just a comment
##### for sonogram calculation #####
BinSono=true
NarrowBoxCar=2.5
BroadBoxCar=5.0
OutputFormat=matlab
OutputDir=/data/sonos
OutputTable=t_tfdisc

# The next two parameters can have values
# displacement, velocity, or acceleration
DataTypeIn=velocity
DataTypeOut=velocity
WindowSlide=20.0
WTimeLength=2.0
LowFreq=10.0
HighFreq=35.0
TimeBandwidth=4.0
#####
```

PARAMETERS

FIRST SECTION

All parameters in this section are not used by the **sono** program itself, but are passed to the **Libgdi** and **Libwfm** libraries. **Sono** only provides minimal checking of these parameters, and relies on the error handling capabilities of the libraries to deal with improper input.

account=char

User name as a login account in the database.
 Use double quotes around the character string.
 Example for SYBASE : account="nrdc"
 Example for ORACLE : account="nrdc/nrdc@t:nrd:dev713"

chan_list=char

Contains the name of the channel from which a sonogram is to be calculated.

Use double quotes around the character string.

Example: `chan_list="HSSE"`

See also **libwfm(3)**

duration=double

Desired length (in seconds) of the seismogram from which to calculate the sonogram, starting from the time specified as **start_time**.

Either **duration** or **end_time** should be specified, but not both.

Example: `duration=35.0`

See also **libwfm(3)**

end_time=double

Desired **end_time** for the seismogram and sonogram (in seconds).

Either **duration** or **end_time** should be specified, but not both.

Example: `end_time=548073352.0`

See also **libwfm(3)**

extension_time=double

Number of seconds to be subtracted from **start_time** and added to **end_time** before searching the `wfdisc` table (in order to make the search more efficient.) A good default value to use should be of the order of minutes.

Example: `extension_time=360`

See also **libwfm(3)**

in_db=char/char

Input database account and password

Example for SYBASE: `in_db=nrdc/nrdc`

Example for ORACLE: `in_db=nrdc/nrdc@t:nrd:dev713`

See also **libwfm(3)**

join=int

Can be set to 0, 1, 2. The default value of 0 does not allow adjacent waveforms to be concatenated. A value of 1 means that input waveform data adjacent in time are joined and indexed through one output `wfdisc`. Time gaps will be filled with values defined by the default **fill_value** used in the **Libwfm** library, namely -1.0. A value of 2 requests that a conditional join be performed, i.e. adjacent waveform data will be joined provided the time gap between them is less than **gapecpsilon**, which is defaulted to the inverse of the sampling rate as per the **Libwfm** convention. A value of 2 is preferred unless the user is sure that another choice is better.

Example: `join=2`

See also **libwfm(3)**

password=char

User password for the login account in the database.

Use double quotes around the character string.

Example: `password="nrdc"`

sta_list=char

Contains the name of the station of interest.

Use double quotes around the character string.

Example: `sta_list="BAY"`

See also **libwfm(3)**

start_time=double

The beginning time of interest for the calculation of the sonogram (in seconds).

This is an epoch time.

Example: start_time=548073338.0

vendor=char

Vendor name for the database.

Tested databases: oracle, sybase.

Use double quotes around the character string.

Example: vendor="sybase"

verbose

Flag. When used, the information about the **libwfm** run is printed to stdout. To suppress the printing don't set this flag.

Example: verbose

See also **libwfm(3)**

wfd_to_wfm

Flag. Indicates that the created wfmem information must be stored in core memory. Required.

Example: wfd_to_wfm

See also **libwfm(3)**

SECOND SECTION

For parameters in this section the **sono** program provides an error check for their names and values, and issues a diagnostic error message.

BinSono=boolean

Boolean flag, takes values **true** or **false** case insensitive. When set to **true** the sonogram is converted to a matrix of values of +1 or -1, (labeled **binary sonogram** by Hedlin et al., 1989) according an the algorithm outlined in the DESCRIPTION section below. Otherwise sonogram values are left as double precision numbers.

Example: BinSono=false

NarrowBoxCar=double

This parameter is required only if **BinSono=true**. Indicates a length (in seconds) of a narrow boxcar function used to smooth each spectrum prior to conversion to a **binary sonogram**

Example: NarrowBoxCar=2.5

BroadBoxCar=double

This parameter is required only if **BinSono=true**. Indicates a length (in seconds) of a broad boxcar function used to smooth each spectrum prior to conversion to a **binary sonogram**

Example: BroadBoxCar=5.0

OutputFormat=char

Specifies the output format of the sonogram. Case insensitive. Available formats are matlab, binary, ascii. See section OUTPUT of this man page for formats details.

Example: OutputFormat=matlab

OutputDir=char

Full path name of a directory where the resulting sonogram is placed.
Example: OutputDir=/data/sonograms/1995/binary_sonos

OutputTable=char

Name of the database table which is updated with information about the calculated sonogram. For this purpose a new table **tfdisc** (according to CSS 3.0 convention) was designed. See section TFDISC TABLE of this man page.
Example: OutputTable=tfdisc

DataTypeIn=char

Flag indicating what type of data is indexed by the wfdisc entry. This flag is used to indicate the natural units of the detector.
Allowed values are displacement, velocity and acceleration.
Example: DataTypeIn=velocity

DataTypeOut=char

Flag indicating what type of data will be written to the resulting sonogram. Allowed values are displacement, velocity and acceleration.
Example: DataTypeOut=velocity

WindowSlide=double

Indicates by how much to shift the time window for successive spectra in the sonogram, as a percentage of window length.
Example: WindowSlide=20.0

WTimeLength=double

Size of the time window (in seconds) used to compute the successive spectra in the sonogram.
Example: WTimeLength=2.0

LowFreq=double

Lower limit of the frequency range of interest. Negative input is reset to 0.0
Example: LowFreq=10.0

HighFreq=double

Upper limit of the frequency range of interest.
Example: HighFreq=35.0

TimeBandwidth=4.0

Time bandwidth used ...
Example: TimeBandwidth=4.0

OUTPUT

The main output of **sono** is a sonogram, in one of several user specifiable formats. In addition, the program updates the database table tfdisc with appropriate indexing (or header) information. (See section TFDISC TABLE below for details on the tfdisc contents.)

The file name is constructed from the station and channel names, and waveform date and start time used in the sonogram calculation. Our present convention produces file names of the form :

sta_chan_yyyyddhhmmss.tf, where

sta – station name

chan – channel name

yyyy – year
 ddd – julian day
 hh – hours
 mm – minutes
 ss – seconds

Currently one of three different formats may be selected: **matlab**, **binary**, **ascii**. The program architecture allows easy expansion for additional user's formats. If such need arises the appropriate additions should be made to the functions `map_format_type()`, `unmap_format_type()` in the file `mapping.c`, and to the function `write_sono()` in the file `write_sono.c`.

In the current formats **Nrows** is the number of frequencies and **Ncolumns** is the number of time windows used for the calculations. Each data point in the matrix is an 8-byte double precision number (in case **BinSono=false**) or 4-byte signed integer (in case **BinSono=true**)

matlab –

The sonogram file structure is that of a Level 1.0 MAT-file. The file consists of a 2-part header followed by the matrix of sonogram data points.

The first part of the header is a standard 20-byte matlab header which consists of 5 four-byte long integers:

1. type –

type flag. An integer whose 4 decimal digits encode storage information. The first digit indicates the numeric format of binary numbers on the computer that wrote the file. **Sono** uses 1, indicating IEEE Big Endian (Macintosh, SPARC, Apollo, SGI, HP9000/300). Other values can be obtained from the matlab documentation if the software is to be ported to a computer with a different architecture. The second digit is always 0. The third digit can take one of two values: 0 - which means that data are stored as double precision, this is when no conversion to a **binary sonogram** was specified. 2 - data are stored as signed integers, this is when the conversion to a **binary sonogram** was requested. The fourth digit is 0 which merely indicates that the matrix is numeric instead of consisting of text items. To summarize, the **sono** program uses two types, both defined in **sono.h**.

type=1020 – when writing double precision values and

type=1000 – when writing signed integer values.

2. Nrows –

number of rows in the matrix.

3. Ncolumns –

number of columns in the matrix.

4. Iflag –

imaginary flag. Always 0 since the resulting sonogram has no imaginary part, only real.

5. NameLength –

number of bytes to hold the matrix name plus 1 byte for the NULL character.

The second part of the header contains a matrix name + 1 for the NULL character. The matrix name is defined in **sono.h** file by **MATNAME**. Total size of the header is <20 + namelength + 1> bytes. This name is of no importance to the analyst, but may be used and/or modified by

MATLAB users to manipulate the matrix.

Sonogram data points are stored in the file immediately after the header as a matrix. The matrix consists of **Nrows** * **Ncolumns** numbers which are stored column-wise in binary format.

binary -

The output file consists of the sonogram points presented as a matrix, where **Nrows** * **Ncolumns** numbers are stored column-wise. Each number requires 8 bytes for double precision or 4 bytes for signed integer. With this choice the output file contains no header and it is assumed that the proper indexing is done exclusively through the DBMS entry in the **tfdisc** table.

ascii - The output file consists of the sonogram points presented as a matrix, where **Nrows** * **Ncolumns** numbers are stored column-wise and written in the file one per line in the format "%15.7E\n" for double precision or "%d" for signed integer. With this choice the output file contains no header and it is assumed that the proper indexing is done exclusively through the DBMS entry in the **tfdisc** table.

DESCRIPTION

The purpose of the sonogram software is to expand time series into 2-dimensional displays which show the dependence of spectral energy on time and frequency. Our research into the time-frequency characteristics of single and multiple chemical explosions detonated and recorded in Kazakhstan, FSU (Hedlin et al., 1989) indicates that a time-independent spectral modulation can be caused by ripple-firing (a blasting technique in which a number of closely grouped explosions are detonated in rapid sequence).

The sonogram software expands a time series into a time-frequency display by using a multi-taper spectral estimation procedure. Successive spectral estimates are obtained from data isolated by a sliding window. Multi-taper spectral estimation has been used because of the proven ability of this approach to yield minimally biased spectral estimates from short time series. See Park et al. (1987) for an explanation of this technique.

Given the complex nature of most spectral estimates we have introduced the option to reduce the sonograms to **binary form**. In this processing each spectral estimate is converted into two smoothed versions which are sensitive to small- and large-scale spectral features. These versions are obtained by convolving the spectral estimate with a short and long boxcars respectively.

By differencing the two estimates and replacing the difference at each frequency with a **+1** to indicate locally high power and a **-1** to indicate the opposite we convert the original spectral estimate into a binary spectral estimate. Applying this, highly non-linear, processing to each individual spectral estimate in the sonogram yields a two-dimensional binary pattern. In Hedlin et al. (1989, 1990) we found that this processing aided discrimination by suppressing minor spectral details and thus enhancing any time-independent spectral signature that might be present.

Given the density of seismic stations in some areas (due to regional networks or arrays) many seismic events are redundantly recorded. As a result it is possible to enhance the time-frequency spectral estimates by stacking. As discussed in Hedlin et al. (1990), stacking can be performed in many ways (e.g. before or after conversion to **binary form**). It has not been proven which approach is best. As a result we have not included this capability in this version of the sonogram software. Stacking sonogram matrices is easily performed within matlab.

FILES

sono.h	include file for C-source files
sono_f77.h	include file for FORTRAN-sources files

db_tfdisc.h definition of a **tfdisc** structure

DIAGNOSTICS

The routines produce error messages on stderr. Most messages report the function that was active when the error have occurred.

LIMITATIONS

This code does not provide for interactive selection of time windows, etc. This choice is deliberate, because a graphical interface should be provided by existing modules at the time of integration with other software.

Pre-processing steps such as frequency-filtering of the waveform data prior to sonogram calculation are assumed to have been accomplished using other modules. If necessary the code could be altered to accommodate such tasks. This would be best done at integration time, since the appropriate modules would not have to be duplicated.

Similarly, stacking of the resulting sonograms, or beamforming prior to sonogram calculation is not provided as part of this code. Such steps are application and user-dependent, and are best accomplished within other modules, or even in the context of other general-purpose packages such as MATLAB.

BUGS

No known bugs at this point.

Report bugs to nwilliams@ucsd.edu

LANGUAGE INTERFACE

C, FORTRAN

SEE ALSO

Hedlin, M. A. H., Minster, J. B., & Orcutt, J. A., 1989. The time-frequency characteristics of quarry blasts and calibration explosions recorded in Kazakhstan, USSR, *Geophysical Journal International*, **99**, 109-121.

Hedlin, M.A.H., Minster, J.B. & Orcutt, J.A., 1990. An automatic means to discriminate between earthquakes and quarry blasts, *Bull. Seismol. Soc. Am.*, **80**, 2143-2160.

Park, J., Lindberg, C.R. and Vernon, F.L., 1987. Multitaper spectral analysis of high-frequency seismograms, *J. Geophys. Res.*, **92**, 12675-12684.

libwfm(3), libwfdisc(3)

AUTHOR

Michael A.H. Hedlin, UCSD/SIO/IGPP, San Diego, CA 92093-0225

Nadya P. Williams, UCSD/SIO/IGPP, San Diego, CA 92093-0225

APPENDIX

TFDISC TABLE

The following contains the description of a new table intended as an extension to the CSS 3.0 database schema, to describe sonograms. **sono** updates this relation automatically when a sonogram is calculated. **Sono** supports either the ORACLE or SYBASE DBMS, through the SAIC Generic Database Interface (GDI). The new table is meant to describe a general time-frequency representation of a time series.

Relation : tfdisc

Description : sonogram file header and descriptive information

Columns Description:

1 - Attribute NAME

2 – Field Number
 3 – Storage Type
 4 – External Format
 5 – Character Position
 6 – Attribute Description

1	2	3	4	5	6
sta	1	c6	a6	1–6	station
chan	2	c8	a8	8–15	channel
time	3	f8	f17.5	17–33	epoch time
tfid	4	i4	i8	35–42	sonogram id
jdate	5	i4	i8	44–51	julian date
dsono	6	f8	f9.2	53–61	duration of sonogram
dwind	7	f8	f6.2	63–68	duration of each window
pslide	8	f8	f5.1	70–74	offset between windows
nt	9	i4	i4	76–79	number of time windows
fmin	10	f8	f7.4	81–87	minimum frequency
fmax	11	f8	f7.4	89–95	maximum frequency
nf	12	i4	i4	97–100	number of frequencies
tbprod	13	f8	f5.2	102–106	time–bandwidth product
neigspect	14	i4	i4	108–111	number of eigenspectra
spectype	15	c2	a2	113–114	spectrum type
bbroad	16	f8	f4.1	116–119	broad boxcar filter
bnarrow	17	f8	f4.1	121–124	narrow boxcar filter
foff	18	i4	i4	126–129	byte offset
dir	19	c64	a64	131–194	directory
dfile	20	c32	a32	196–227	tf file
tfformat	21	c9	a9	229–237	tf file format
progver	22	c15	a15	239–253	program identifier
lddate	23	date	a17	255–271	load date

TFDISC TABLE ATTRIBUTES

Name:	sta
Description:	Station code. This is a common code–name of seismic observatory. Usually 3 or 4 characters are used.
ORACLE:	VARCHAR(6)
SYBASE:	VARCHAR(6)
NA Value:	A valid entry is required.
Range:	Any upper case string up to 6 characters long.
Name:	chan
Description:	Channel identifier. This is an eight–character code which, taken together with sta and time, uniquely identifies the source of the seismic data.
ORACLE:	VARCHAR(8)
SYBASE:	VARCHAR(8)
NA Value:	A valid entry is required.
Range:	Any upper case string up to 6 characters long.

Name:	time
Description:	Epoch time. Given in seconds and fractions of a second since hour 0 January 1, 1970. Stored in a double precision floating point number.
ORACLE:	FLOAT(53)
SYBASE:	FLOAT
NA Value:	A valid entry is required.
Units:	Seconds
Name:	tfid
Description:	Sonogram identifier. The key field is a unique identifier for a sonogram calculated for a certain segment of waveform data.
ORACLE:	NUMBER(8)
SYBASE:	INT
NA Value:	A valid entry is required.
Range:	tfid > 0
Name:	jdate
Description:	Julian date. This attribute is the date of an onset of a P-wave for a certain segment of waveform data for which the sonogram was calculated.
ORACLE:	NUMBER(8)
SYBASE:	INT
NA Value:	A valid entry is required.
Range:	Julian dates of the form yyyyddd. Must be consistent with the accompanying time attribute.
Name:	dsono
Description:	Duration of the waveform to use for the sonogram calculation.
ORACLE:	FLOAT(24)
SYBASE:	FLOAT
NA Value:	A valid entry is required.
Range:	A positive integer. Generally a value less than 35 may not give a good sonogram.
Units:	Seconds
Name:	dwind
Description:	Duration of a time window during the sonogram calculation.
ORACLE:	FLOAT(24)
SYBASE:	FLOAT
NA Value:	A valid entry is required.
Range:	A positive value of the order of a few seconds.
Units:	Seconds
Name:	pslide
Description:	Offset between windows as a percent of a window duration.
ORACLE:	FLOAT(24)
SYBASE:	FLOAT

NA Value: valid value is required
 Range: $0 < \text{pslide} < \text{dwind}$
 Units: percent

Name: **nt**
 Description: Number of the time windows used for the calculation of the sonogram.
 ORACLE: FLOAT(24)
 SYBASE: FLOAT
 NA Value: A valid entry is required.
 Range: $\text{nt} > 1$

Name: **fmin**
 Description: Minimum frequency used for the calculation of the sonogram
 ORACLE: FLOAT(24)
 SYBASE: FLOAT
 NA Value: A valid entry is required
 Range: $0.0 \leq \text{fmin} < \text{fmax}$
 Units: Hertz

Name: **fmax**
 Description: Maximum frequency used for the calculation of the sonogram
 ORACLE: FLOAT(24)
 SYBASE: FLOAT
 NA Value: A valid entry is required.
 Range: $\text{fmin} < \text{fmax} \leq \text{Nyquist frequency}$
 Units: Hertz

Name: **nf**
 Description: Number of frequencies used for the calculation of the sonogram
 ORACLE: FLOAT(24)
 SYBASE: FLOAT
 NA Value: A valid entry is required
 Range: Is calculated by the program from dwind , fmax , fmin and, if exist, bbroad and bnarrow .

Name: **tbprod**
 Description: time-bandwidth product
 ORACLE: FLOAT(24)
 SYBASE: FLOAT
 NA Value: A valid value is required.
 Range: $\text{tbprod} > 0$

Name: **neigspect**
 Description: Number of Eigen spectra.
 ORACLE: FLOAT(24)
 SYBASE: FLOAT
 NA Value: A valid value is required
 Range: Is calculated by the program from tbprod as $\langle 2 * \text{tbprod} - 1 \rangle$

Name:	spectype
Description:	Flag indicating what type of data is written to the resulting sonogram, and whether the conversion to the binary sonogram was performed
ORACLE:	VARCHAR(2)
SYBASE:	VARCHAR(2)
NA Value:	A valid entry is required
Range:	{ bd bv ba d v a }, lower case These flags stand for : bd – data type displacement, conversion to binary sonogram bv – data type velocity, conversion to binary sonogram ba – data type acceleration, conversion to binary sonogram d – data type displacement, no conversion to binary sonogram v – data type velocity, no conversion to binary sonogram a – data type acceleration, no conversion to binary sonogram

Name:	bbroad
Description:	This is a length of a broad boxcar function used to smooth each spectrum prior to conversion to binary sonogram
ORACLE:	FLOAT(24)
SYBASE:	FLOAT
NA Value:	A valid entry is required
Range:	bnarrow < bbroad < (fmax – fmin) If no BinSono was specified then this value is 0.0.
Units:	Hertz

Name:	bnarrow
Description:	This is a length of a narrow boxcar function used to smooth each spectrum prior to conversion to binary sonogram
ORACLE:	FLOAT(24)
SYBASE:FLOAT	
NA Value:	A valid entry is required
Range:	0.0 < bnarrow < bbroad If no BinSono was specified then this value is 0.0.
Units:	Hertz

Name:	foff
Description:	File offset. This is the byte offset (header size) of the data segment within a sonogram.
ORACLE:	NUMBER(8)
SYBASE:	INT
NA Value:	A valid value is required
Range:	foff ≥ 0

Name: **dir**
Description: Directory. A directory part of the a path name to the location of the created sonogram. A relative path or a "." may be used.
ORACLE: VARCHAR(64)
SYBASE: VARCHAR(64)
NA Value: A valid value is required.
Range: Any string up to 64 characters long, where each character is a legal character for a directory name under UNIX.

Name: **dfile**
Description: File name. This is the name of the sonogram file.
ORACLE: VARCHAR(32)
SYBASE: VARCHAR(32)
NA Value: A valid entry is required.
Range: Any string up to 32 characters long, where each character is a legal character for a file name under UNIX.

Name: **tfformat**
Description: Output format name. A name of a format used to write the calculated sonogram.
ORACLE: VARCHAR(10)
SYBASE: VARCHAR(10)
NA Value: A valid entry is required.
Range: { matlab | binary | ascii }, lower case

Name: **progver**
Description: Identifier for the program's version.
ORACLE: VARCHAR(10)
SYBASE: VARCHAR(10)
NA Value: A valid entry is required
Range: Any string of 10 characters which specifies the version and the name

Name: **lddate**
Description: Load date This is the date and time when the record was inserted into the table.
ORACLE: DATE
SYBASE: DATETIME
NA Value: A valid entry is required
Range: Any valid date

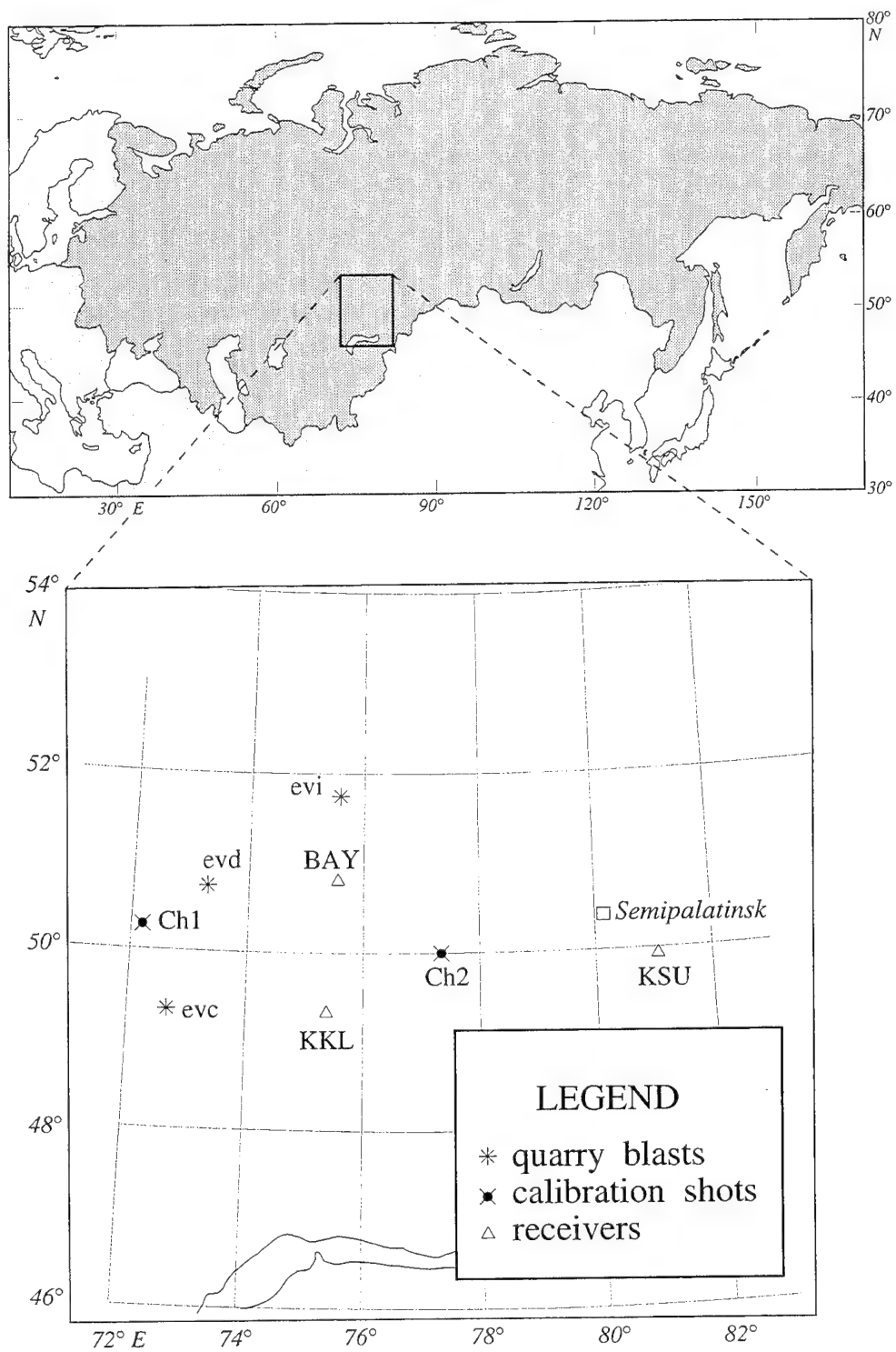


Figure A1. Geographic locations of receivers and events in the 1989 NRDC dataset.

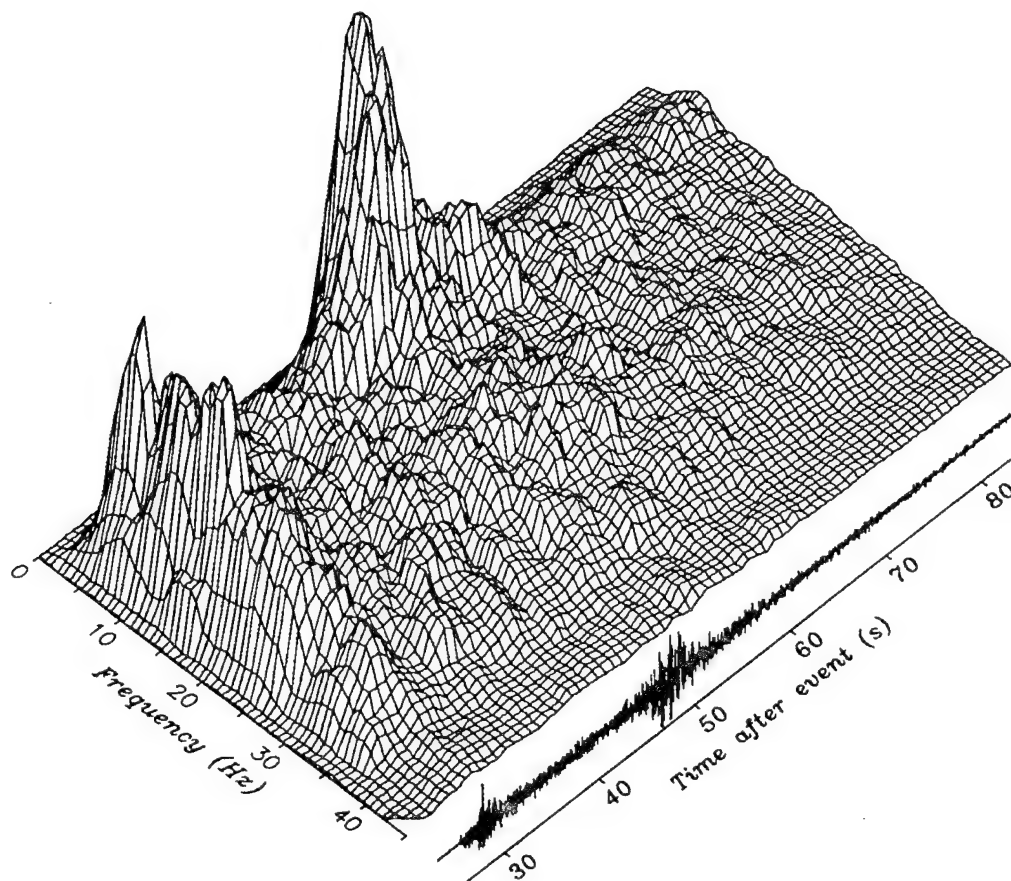


Figure A2. Seismogram resulting from the single-chemical explosion Chemex 2 recorded at a range of 157 km by the vertical component surface seismometer at Bayanaul and corresponding sonogram.

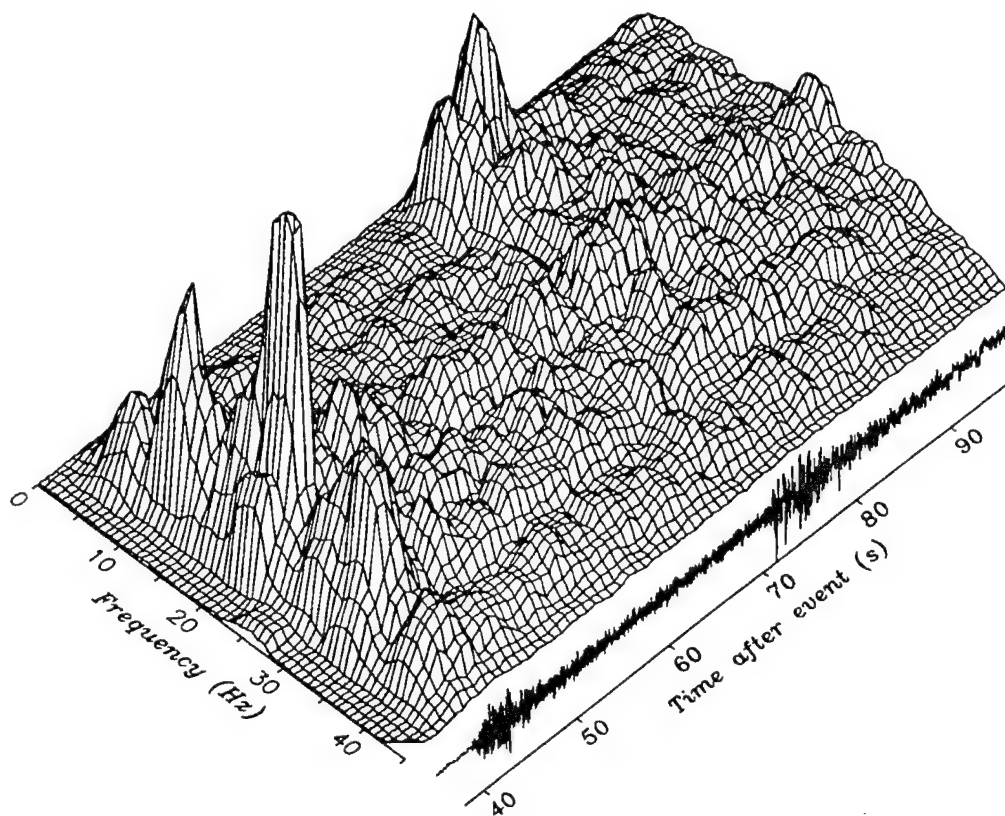


Figure A3. Seismogram resulting from event c recorded at a range of 264 km by the vertical component surface seismometer at Bayanaul and corresponding sonogram. This event is believed to be ripple fired. The sonogram matrix contains a clear time-independent spectral signature.

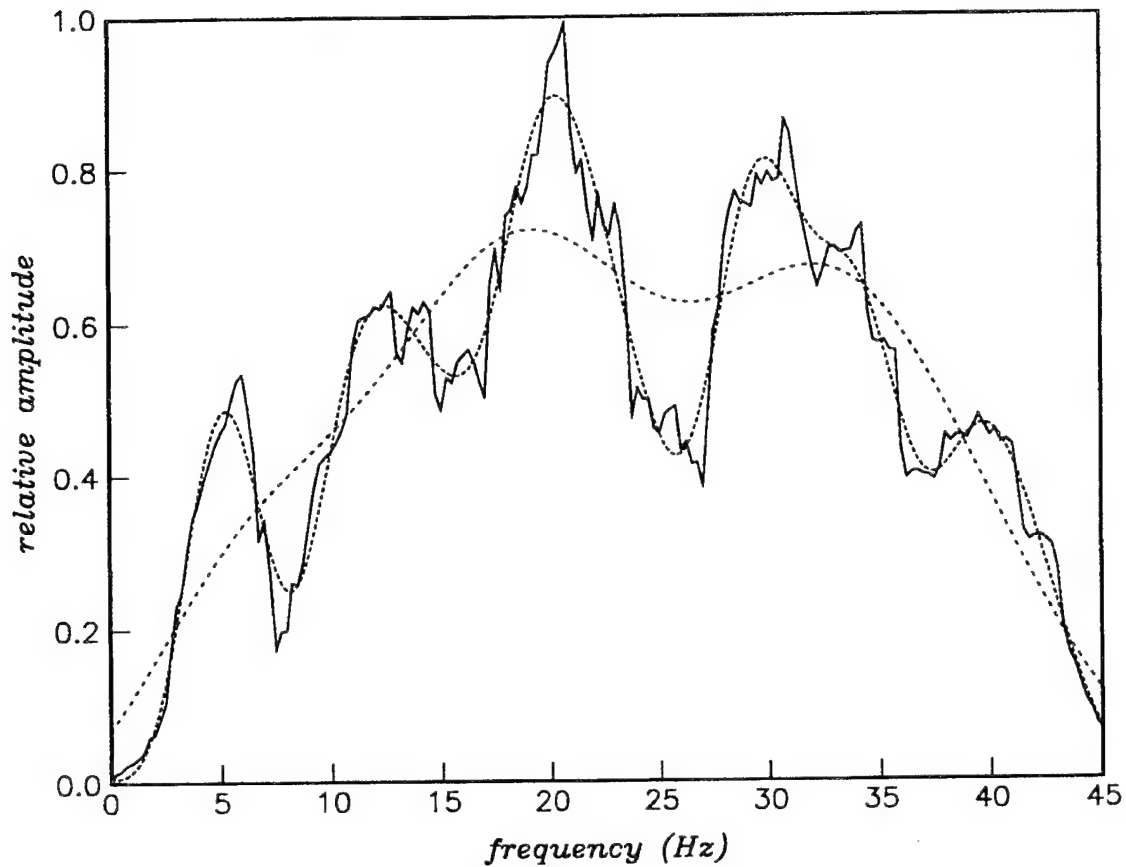


Figure A4. Original spectral estimate (solid) and two filtered versions, one relatively unsmoothed (fine dash) and the other heavily smoothed (coarse dash). This figure is intended to illustrate the means by which we reduce each spectral estimate to a binary spectral estimate. In the following figures regions of locally high power are represented by a +1 (white). Regions deficient in power are represented by a -1 (black).

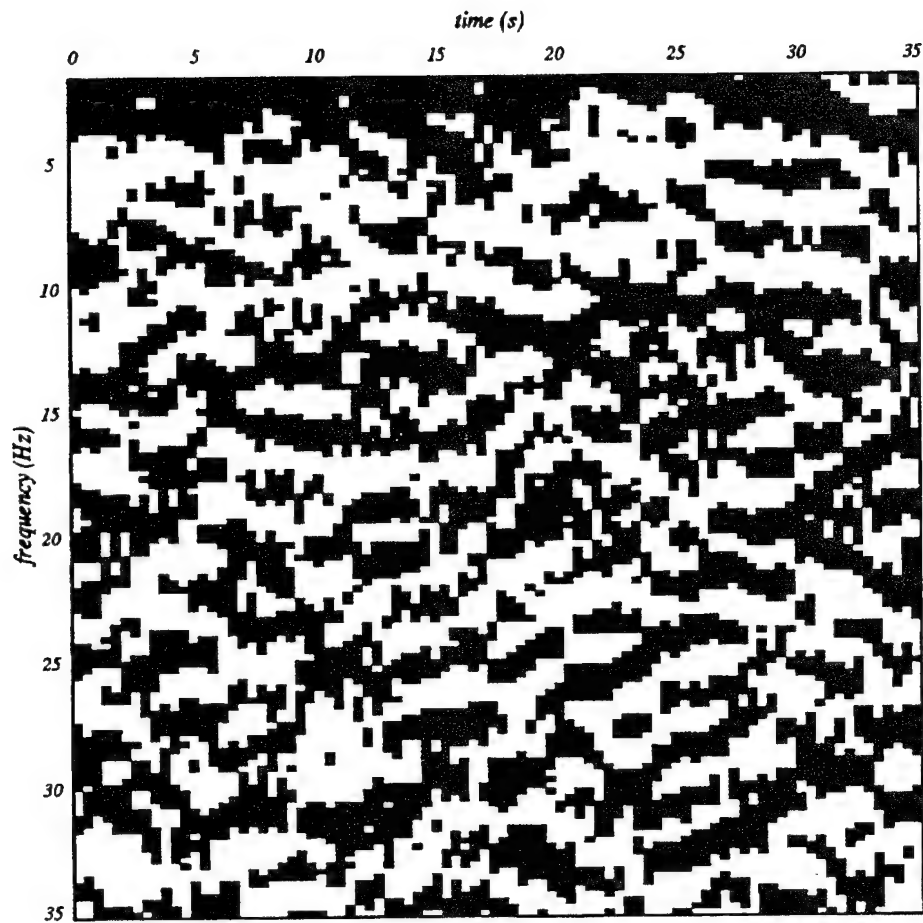


Figure A5. Vertical component binary sonogram matrix corresponding to Chemex 2 recorded at Bayanaul (see Figure 2). The first 35 seconds of coda after the compressional onset are represented in this and the next binary sonogram.

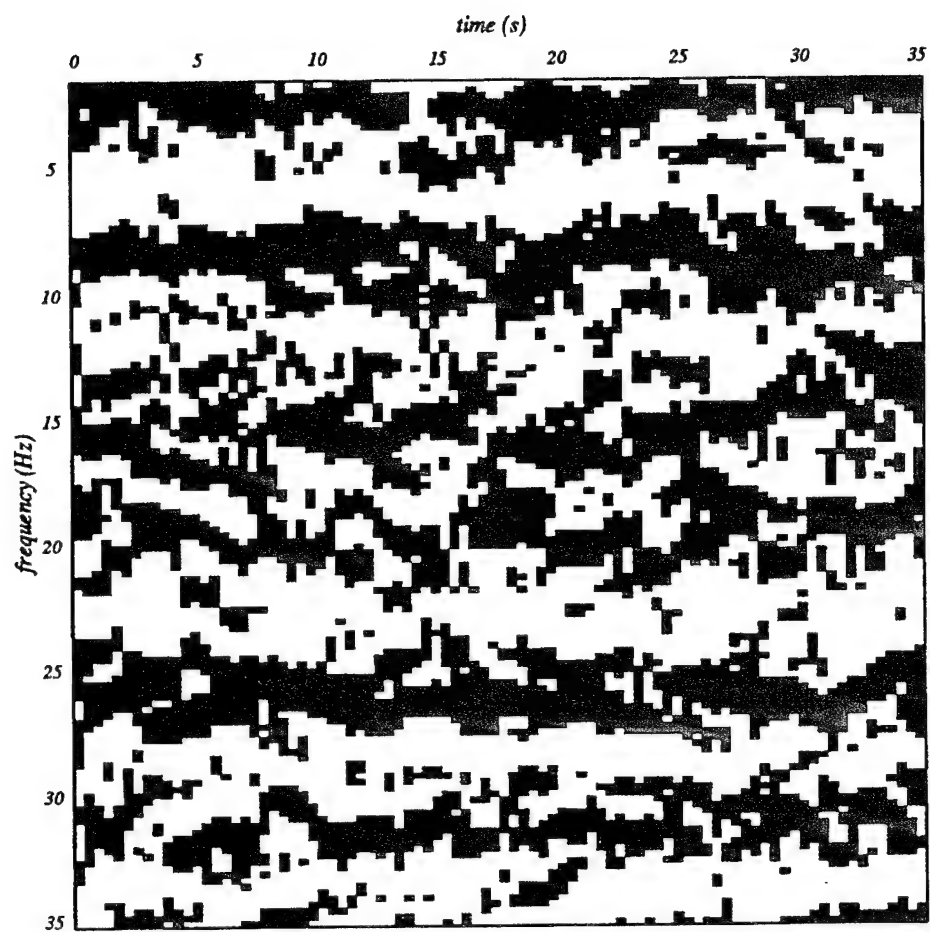


Figure A6. Vertical component binary sonogram matrix corresponding to event c recorded at Bayanaul (see Figure 3). Note the clear time-independent pattern.

Prof. Thomas Ahrens
Seismological Lab, 252-21
Division of Geological & Planetary Sciences
California Institute of Technology
Pasadena, CA 91125

Prof. Keiiti Aki
Center for Earth Sciences
University of Southern California
University Park
Los Angeles, CA 90089-0741

Prof. Shelton Alexander
Geosciences Department
403 Deike Building
The Pennsylvania State University
University Park, PA 16802

Dr. Thomas C. Bache, Jr.
Science Applications Int'l Corp.
10260 Campus Point Drive
San Diego, CA 92121 (2 copies)

Prof. Muawia Barazangi
Cornell University
Institute for the Study of the Continent
3126 SNEE Hall
Ithaca, NY 14853

Dr. Douglas R. Baumgardt
ENSCO, Inc
5400 Port Royal Road
Springfield, VA 22151-2388

Dr. T.J. Bennett
S-CUBED
A Division of Maxwell Laboratories
11800 Sunrise Valley Drive, Suite 1212
Reston, VA 22091

Dr. Robert Blandford
AFTAC/TT, Center for Seismic Studies
1300 North 17th Street
Suite 1450
Arlington, VA 22209-2308

Dr. Stephen Bratt
ARPA/NMRO
3701 North Fairfax Drive
Arlington, VA 22203-1714

Mr. Dale Breeding
Sandia National Laboratories
Organization 9236, MS 0655
Albuquerque, NM 87185

Dr. Jerry Carter
Center for Seismic Studies
1300 North 17th Street
Suite 1450
Arlington, VA 22209-2308

Mr Robert Cockerham
Arms Control & Disarmament Agency
320 21st Street North West
Room 5741
Washington, DC 20451,

Dr. Zoltan Der
ENSCO, Inc.
5400 Port Royal Road
Springfield, VA 22151-2388

Dr. Stanley K. Dickinson
AFOSR/NM
110 Duncan Avenue
Suite B115
Bolling AFB, DC 20332-6448

Dr. Petr Firbas
Institute of Physics of the Earth
Masaryk University Brno
Jecna 29a
612 46 Brno, Czech Republic

Dr. Mark D. Fisk
Mission Research Corporation
735 State Street
P.O. Drawer 719
Santa Barbara, CA 93102

Dr. Cliff Frolich
Institute of Geophysics
8701 North Mopac
Austin, TX 78759

Dr. Holly Given
IGPP, A-025
Scripps Institute of Oceanography
University of California, San Diego
La Jolla, CA 92093

Dr. Jeffrey W. Given
SAIC
10260 Campus Point Drive
San Diego, CA 92121

Dan N. Hagedorn
Pacific Northwest Laboratories
Battelle Boulevard
Richland, WA 99352

Dr. James Hannon
Lawrence Livermore National Laboratory
P.O. Box 808, L-205
Livermore, CA 94550

Dr. Roger Hansen
University of Colorado, JSPC
Campus Box 583
Boulder, CO 80309

Prof. David G. Harkrider
Phillips Laboratory
Earth Sciences Division, PL/GPE
29 Randolph Road
Hanscom AFB, MA 01731-3010

Prof. Danny Harvey
University of Colorado, JSPC
Campus Box 583
Boulder, CO 80309

Prof. Donald V. Helmberger
Division of Geological & Planetary Sciences
California Institute of Technology
Pasadena, CA 91125

Prof. Eugene Herrin
Geophysical Laboratory
Southern Methodist University
Dallas, TX 75275

Prof. Robert B. Herrmann
Department of Earth & Atmospheric Sciences
St. Louis University
St. Louis, MO 63156

Prof. Lane R. Johnson
Seismographic Station
University of California
Berkeley, CA 94720

Prof. Thomas H. Jordan
Department of Earth, Atmospheric &
Planetary Sciences
Massachusetts Institute of Technology
Cambridge, MA 02139

Mr. Robert C. Kemerait
ENSCO, Inc.
445 Pineda Court
Melbourne, FL 32940

U.S. Dept of Energy
Max Koontz, NN-20, GA-033
Office of Research and Develop.
1000 Independence Avenue
Washington, DC 20585

Dr. Richard LaCoss
MIT Lincoln Laboratory, M-200B
P.O. Box 73
Lexington, MA 02173-0073

Prof. Charles A. Langston
Geosciences Department
403 Deike Building
The Pennsylvania State University
University Park, PA 16802

Jim Lawson, Chief Geophysicist
Oklahoma Geological Survey
Oklahoma Geophysical Observatory
P.O. Box 8
Leonard, OK 74043-0008

Prof. Thorne Lay
Institute of Tectonics
Earth Science Board
University of California, Santa Cruz
Santa Cruz, CA 95064

Dr. William Leith
U.S. Geological Survey
Mail Stop 928
Reston, VA 22092

Mr. James F. Lewkowicz
Phillips Laboratory/GPE
29 Randolph Road
Hanscom AFB, MA 01731-3010(2 copies)

Dr. Gary McCartor
Department of Physics
Southern Methodist University
Dallas, TX 75275

Prof. Thomas V. McEvelly
Seismographic Station
University of California
Berkeley, CA 94720

Dr. Keith L. McLaughlin
S-CUBED
A Division of Maxwell Laboratory
P.O. Box 1620
La Jolla, CA 92038-1620

Prof. Bernard Minster
IGPP, A-025
Scripps Institute of Oceanography
University of California, San Diego
La Jolla, CA 92093

Prof. Brian J. Mitchell
Department of Earth & Atmospheric Sciences
St. Louis University
St. Louis, MO 63156

Mr. Jack Murphy
S-CUBED
A Division of Maxwell Laboratory
11800 Sunrise Valley Drive, Suite 1212
Reston, VA 22091 (2 Copies)

Dr. Keith K. Nakanishi
Lawrence Livermore National Laboratory
L-025
P.O. Box 808
Livermore, CA 94550

Prof. John A. Orcutt
IGPP, A-025
Scripps Institute of Oceanography
University of California, San Diego
La Jolla, CA 92093

Dr. Howard Patton
Lawrence Livermore National Laboratory
L-025
P.O. Box 808
Livermore, CA 94550

Dr. Frank Pilotte
HQ AFTAC/TT
1030 South Highway A1A
Patrick AFB, FL 32925-3002

Dr. Jay J. Pulli
Radix Systems, Inc.
6 Taft Court
Rockville, MD 20850

Prof. Paul G. Richards
Lamont-Doherty Earth Observatory
of Columbia University
Palisades, NY 10964

Mr. Wilmer Rivers
Teledyne Geotech
1300 17th St N #1450
Arlington, VA 22209-3803

Dr. Alan S. Ryall, Jr.
Lawrence Livermore National Laboratory
P.O. Box 808, L-205
Livermore, CA 94550

Dr. Chandan K. Saikia
Woodward Clyde- Consultants
566 El Dorado Street
Pasadena, CA 91101

Mr. Dogan Seber
Cornell University
Inst. for the Study of the Continent
3130 SNEE Hall
Ithaca, NY 14853-1504

Secretary of the Air Force
(SAFRD)
Washington, DC 20330

Office of the Secretary of Defense
DDR&E
Washington, DC 20330

Thomas J. Sereno, Jr.
Science Application Int'l Corp.
10260 Campus Point Drive
San Diego, CA 92121

Dr. Michael Shore
Defense Nuclear Agency/SPSS
6801 Telegraph Road
Alexandria, VA 22310

Prof. David G. Simpson
IRIS, Inc.
1616 North Fort Myer Drive
Suite 1050
Arlington, VA 22209

Dr. Jeffrey Stevens
S-CUBED
A Division of Maxwell Laboratory
P.O. Box 1620
La Jolla, CA 92038-1620

Prof. Brian Stump
Los Alamos National Laboratory
EES-3
Mail Stop C-335
Los Alamos, NM 87545

Prof. Tuncay Taymaz
Istanbul Technical University
Dept. of Geophysical Engineering
Mining Faculty
Maslak-80626, Istanbul Turkey

Prof. M. Nafi Toksoz
Earth Resources Lab
Massachusetts Institute of Technology
42 Carleton Street
Cambridge, MA 02142

Dr. Larry Turnbull
CIA-OSWR/NED
Washington, DC 20505

Dr. Karl Veith
EG&G
2341 Jefferson Davis Highway
Suite 801
Arlington, VA 22202-3809

Prof. Terry C. Wallace
Department of Geosciences
Building #77
University of Arizona
Tucson, AZ 85721

Dr. William Wortman
Mission Research Corporation
8560 Cinderbed Road
Suite 700
Newington, VA 22122

ARPA, OASB/Library
3701 North Fairfax Drive
Arlington, VA 22203-1714

HQ DNA
ATTN: Technical Library
Washington, DC 20305

Defense Technical Information Center
8725 John J. Kingman Road
Ft Belvoir, VA 22060-6218(2 copies)

TACTEC
Battelle Memorial Institute
505 King Avenue
Columbus, OH 43201 (Final Report)

Phillips Laboratory
ATTN: GPE
29 Randolph Road
Hanscom AFB, MA 01731-3010

Phillips Laboratory
ATTN: TSML
5 Wright Street
Hanscom AFB, MA 01731-3004

Phillips Laboratory
ATTN: PL/SUL
3550 Aberdeen Ave SE
Kirtland, NM 87117-5776 (2 copies)

Dr. Michel Campillo
Observatoire de Grenoble
I.R.I.G.M.-B.P. 53
38041 Grenoble, FRANCE

Dr. Kin Yip Chun
Geophysics Division
Physics Department
University of Toronto
Ontario, CANADA

Prof. Hans-Peter Harjes
Institute for Geophysics
Ruhr University/Bochum
P.O. Box 102148
4630 Bochum 1, GERMANY

Prof. Eystein Husebye
IFJF
Jordskjelvstasjonen
Allegaten, 5007 BERGEN NORWAY

David Jepsen
Acting Head, Nuclear Monitoring Section
Bureau of Mineral Resources
Geology and Geophysics
G.P.O. Box 378, Canberra, AUSTRALIA

Ms. Eva Johannisson
Senior Research Officer
FOA
S-172 90 Sundbyberg, SWEDEN

Dr. Peter Marshall
Procurement Executive
Ministry of Defense
Blacknest, Brimpton
Reading FG7-FRS, UNITED KINGDOM

Dr. Bernard Massinon, Dr. Pierre Mechler
Societe Radiomana
27 rue Claude Bernard
75005 Paris, FRANCE (2 Copies)

Dr. Svein Mykkeltveit
NTNT/NORSAR
P.O. Box 51
N-2007 Kjeller, NORWAY (3 Copies)

Dr. Jorg Schlittenhardt
Federal Institute for Geosciences & Nat'l Res.
• Postfach 510153
D-30631 Hannover , GERMANY

Dr. Johannes Schweitzer
Institute of Geophysics
Ruhr University/Bochum
P.O. Box 1102148
4360 Bochum 1, GERMANY

Trust & Verify
VERTIC
Carrara House
20 Embankment Place
London WC2N 6NN, ENGLAND